Supporting Information

Multi-enzyme reaction inspired cascade photocatalysis for solar-driven CO_2 reduction to ethane

Qian Zhang[1⊥], Shuaiqi Gao[1⊥], Xiao Zhao[2], Huiyong Wang[1]*, Yingying Guo[1], Zhimin Liu[3]*, and Jianji Wang[1]*

[1] Key Laboratory of Green Chemical Media and Reactions (Ministry of Education), Collaborative Innovation Centre of Henan Province for Green Manufacturing of Fine Chemicals, School of Chemistry and Chemical Engineering, Henan Normal University, Xinxiang, Henan 453007, P. R. China.
[2] Science and Technology on Aerospace Chemical Power Laboratory, Hubei Institute of Aerospace Chemotechnology, Hubei, 441003, P. R. China.
[3] Beijing National Laboratory for Molecular Sciences, Key Laboratory of Colloid, Interface and Thermodynamics, CAS Research/Education Centre for Excellence in Molecular Sciences, Institute of Chemistry, Chinese Academy of Sciences, Beijing 100190, P. R. China.

[⊥]These authors contributed equally.

*Correspondence authors.
Email: hywang@htu.edu.cn (H. W); liuzm@iccas.ac.cn (Z. L); jwang@htu.edu.cn (J. W)

Table of Contents:

1. Supplementary Methods

Chemicals and POPs synthesis

Chemicals

5,10,15,20-Tetrakis(4-aminophenyl)-21H,23H-porphyrin (TAPP, 97%, Alfa Aesar), 5,5',5''-(benzene-1,3,5-triyl)tripicolinaldehyde (TTPD, 97%, Alfa Aesar), acetonitrile (MeCN, 99%, Keshi), $MoCl_5$ (99.6%, Aladdin), ethanol (99.7%, Keshi), triethanolamine (TEOA, 99%, Aladdin), $Cu(OAc)_2 \cdot H_2O$ (98%, Macklin), tris(2,2'-bipyridyl) ruthenium(II) chloride hexahydrate (98%, Macklin), 1,3,5-trimethylbenzene (98%, Aladdin), $Co(NO)_3 \cdot 6H_2O$ (98 %, Alfa Aesar), methanol (99%, Keshi), 1,4-dioxane (99.7%, Damas-beta), $Ni(OAc)_2 \cdot 4H_2O$ (99%, Macklin), tetrahydrofuran (THF, 99%, Deen reagent), 2,2'-bipyridine (99%, J&K Chemical), $Zn(NO)_3 \cdot 6H_2O$ (99%, Aladdin), and Nafion D520 dispersion solution (DuPont) were used as received. Ar gas (99.99 vol%) and CO_2 gas (99.999 vol%,) were purchased from Xinxiang Yuxin Gas Manufacturing Co. Ltd.

Synthesis of Por-POP-Mo

Por-POP (10.00 mg), $MoCl_5$ (30.00 mg, 0.11 mmol), and 2,2'-bipyridine (17.18 mg, 0.11 mmol) were added to acetonitrile solution under a nitrogen atmosphere. The reaction mixture was refluxed at 95 °C for 24 h. After centrifugation, the resultant powder was washed several times with acetonitrile and methanol successively to ensure the removal of residual metal ions. Finally, the product was dried at 80 °C under vacuum for 12 h. The content of Mo atom was 13.2 wt% as determined by inductively coupled plasma–mass spectrometry.

Materials characterization

Field emission scanning electron microscope (FESEM) images were obtained on JEOL JSM-6390L. Fourier transform infrared (FTIR) spectra were recorded on a Perking Elmer Spectrum 400F spectroscopy. CO_2 adsorption isotherms were measured at 25 ^oC by using a Quantachrome Autosorb-iQ adsorption analyzer after degassing at 200 ^oC for 12 h. X-ray diffraction (XRD) patterns of all sample powders were measured by a X'Pert3 Powder Advance diffractometer with monochromatized

Cu Kα radiation operating at 45 kV and 40 mA. Transmission electron microscope (TEM) images and energy-dispersive X-ray spectra (EDS) were acquired using a JEM-ARM300F electron microscope at 200 kV. The N_2 adsorption and desorption isotherms were determined at -196 ^oC by a Quantachrome Autosorb-iQ adsorption analyzer after degassing at 200 ^oC for 8 h. The Brunauer-Emmet-Teller (BET) and nonlocal density functional theory (NLDFT) models were used to determine specific surface areas and pore size distributions. The inductively coupled plasma-mass spectrum (ICP-MS) of metal elements was recorded on the Agilent 7700 spectroscopy. Thermogravimetric analysis (TGA) was measured from 25 to 600 ^oC under N_2 atmosphere with a heating rate of 10 ^oC min^{-1} using a NETZSCH STA449C thermal analyzer.

The steady-state photoluminescence (PL) spectra and PL decay spectra were measured by a FLS980 Fluorescence Spectrometer (UK). Electrochemical tests were performed by a CHI 660E electrochemical working station (Shanghai). Solid-state UV-vis diffuse reflectance spectra of the samples were collected on a Perkin Elmer Lambda 950 spectroscopy (USA) using $BaSO_4$ as the reference. X-ray photoelectron spectroscopy (XPS) analysis was performed using the Thermo Scientific K-Alpha electron energy spectrometer with Al Kα (1486.6 eV) radiation as the X-ray excitation source and all XPS data were corrected by standard C 1s peak (284.6 eV). The quasi-in-situ XPS spectra were recorded using a Thermo Fisher SCIENTIFIC ESCALAB 250 (USA) spectrometer. X-ray absorption fine structure (XAFS) spectra (Cu K-edge and Mo K-edge) were collected at the 1W1B station in Beijing Synchrotron Radiation Facility (BSRF) operated at 2.5 GeV with a maximum current of 250 mA.

Photoelectrochemical measurements

The photoelectrochemical measurements were carried out with a standard three-electrode system by a Gamry CHI 660E electrochemical workstation. For the three-electrode system, the saturated Ag/AgCl electrode, Pt mesh (1.0×1.0 cm^2), and the photocatalysts modified indium tin oxide (ITO) glass were used as the reference electrode, counter electrode, and working electrode, respectively. For the preparation

of working electrode, 5.00 mg of the as-prepared photocatalyst and 15 μL of Nafion solution were dispersed in 85 μL ethanol, and sonicated for 30 min. Then, the 100 μL photocatalyst colloid was spread evenly on the surface of ITO conductive glass (1.0×1.0 cm^2). After drying in the air at room temperature, the working electrode was stored in petri dishes for related tests. The photoelectric test was carried out in 0.500 M aqueous sodium sulfate solution under light illumination or dark, and 300 W Xe lamp (cut 420 nm) was used as a light source. Mott-Schottky (M-S) plots were determined at the frequencies of 200, 500 and 800 Hz, respectively, and EIS measurements were performed in the frequency range from 10 kHz to 0.1 Hz.

Apparent quantum efficiency of C_2H_6

The apparent quantum efficiency (AQE) was measured under the same photocatalytic reaction conditions irradiated by different wavelengths of light produced from bandpass filters (including 420, 450, 500, 520, 550, 600 and 630 nm) for 2h. The light intensity was detected by a Newport 91150-2000 optical power meter (USA Newport Corporation). The AQE values were calculated according to the below equation [4, 5]:

$$\mathrm{AQE}(\%) = (\text{number of reacted electrons}/\text{number of incident photons}) \times 100\%$$
$$= ((n \times N_A \times h \times c)/(S \times P \times \lambda \times t)) \times 100\% \quad \text{(S3)}$$

where N_A is Avogadro's constant (6.022×10^{23} mol^{-1}), n is the molar number of the C_2H_6, h is the Planck's constant (6.63×10^{-34} m^2 kg s^{-1}), S is the irradiation area (cm^2), c is the speed of light (3×10^8 m s^{-1}), P is irradiation intensity (W cm^{-2}), λ is the wavelength of the light source, and t is irradiation time (s), respectively. Note that the apparent quantum efficiency calculations described above did not consider the catalyst amount and the transparency of the photocatalytic reactor.

Computational Methods

The DFT calculations were performed using the Vienna ab initio simulation package (VASP). The generalized gradient approximation (GGA) with the Perdew–Burke–Emzerhof (PBE) functional [6] was employed to describe the exchange correlation energy. Projector augmented wave (PAW) methods [7] were used for the

pseudopotentials. The energy cutoff for the plane wave basis was set to be 500 eV, and the convergence criterion of geometry relaxation was 0.02 eV/Å in force. For geometric optimization, the energy convergence criterion was set to 1×10^{-5} eV. Meanwhile, the electronic structures of the optimized structures along reaction pathway were also calculated through Gaussian 09 program, where the (U)PBE1PBE hybrid functional [8] was adopted, and the 6-311G** basis set was used for C, H, O and N atoms, the Lanl2DZ basis set was used for Cu and Mo atoms. The free energy diagram for the CO_2 photoreduction pathway was calculated through the VASPKIT tool based on the equation ($\Delta G = \Delta E + \Delta EZPE - T\Delta S$), where ΔE, $\Delta EZPE$, and $T\Delta S$ represent the calculated electronic energy, zero-point energy, and entropy contribution, respectively.

2. Supplementary Figures 1-39

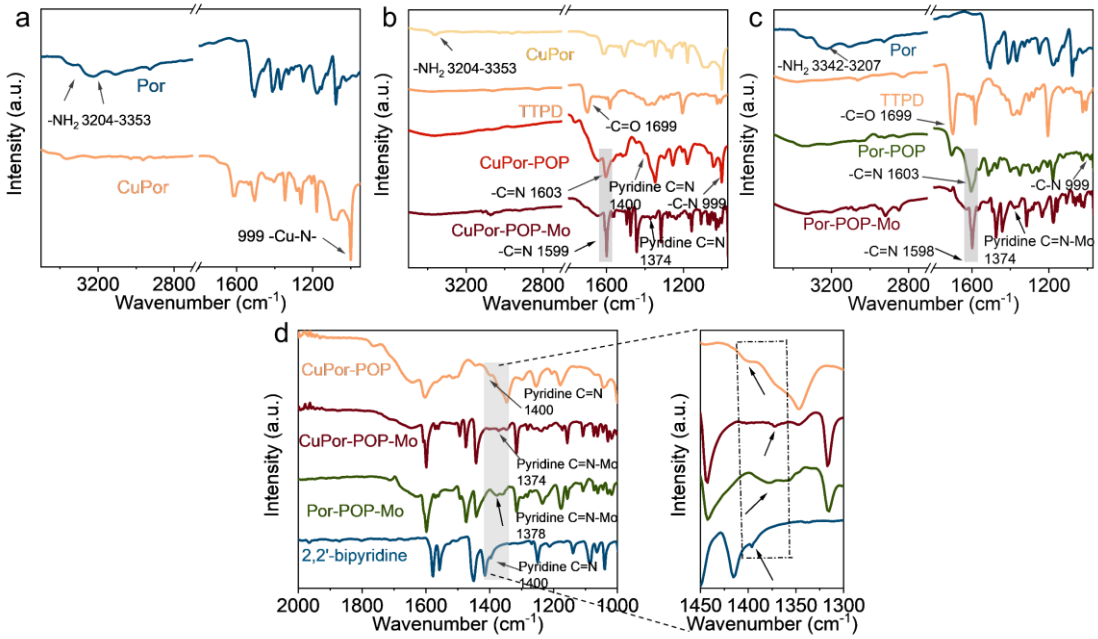

Supplementary Figure 1 FTIR spectra. a CuPor. **b** CuPor-POP and CuPor-POP-Mo. **c** Por-POP and Por-POP-Mo. **d** 2,2'-bipyridine and POPs.

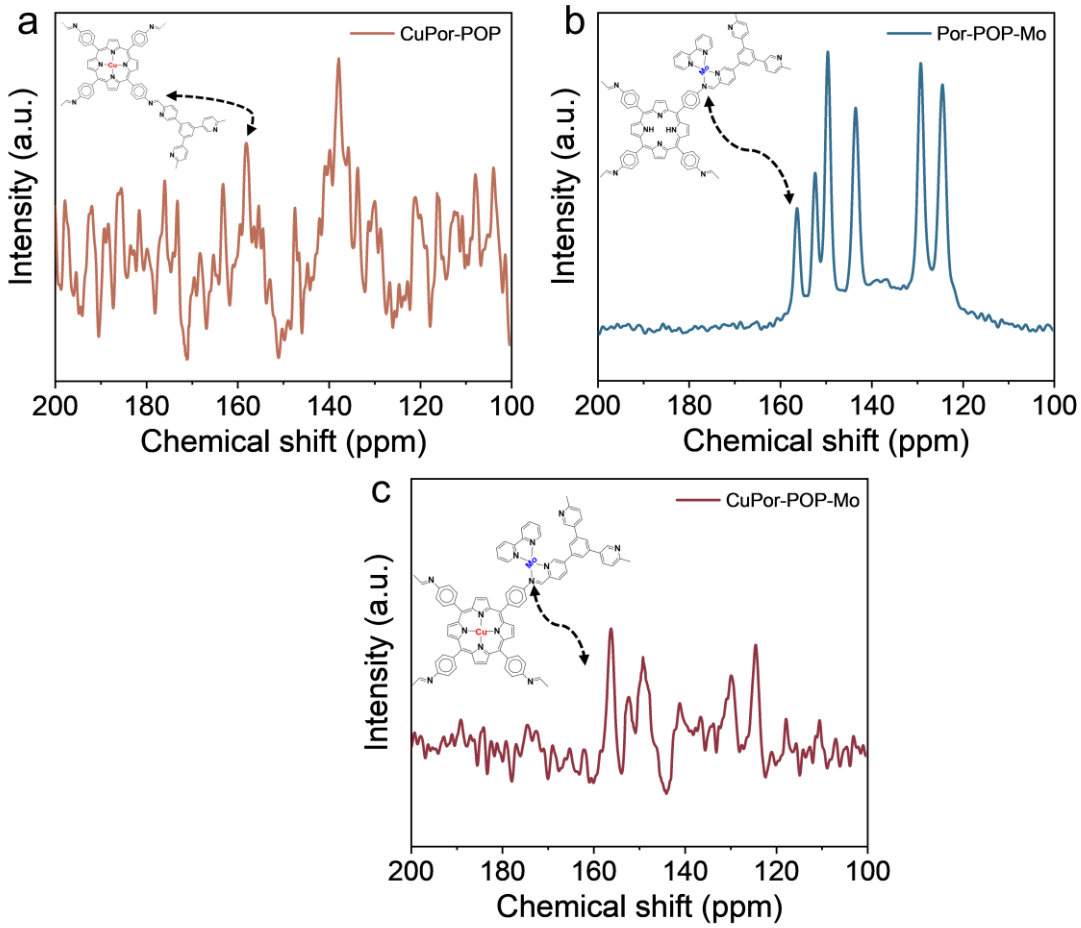

Supplementary Figure 2 Solid state ^{13}C NMR spectra. a CuPor-POP. **b** Por-POP-Mo. **c** CuPor-POP-Mo.

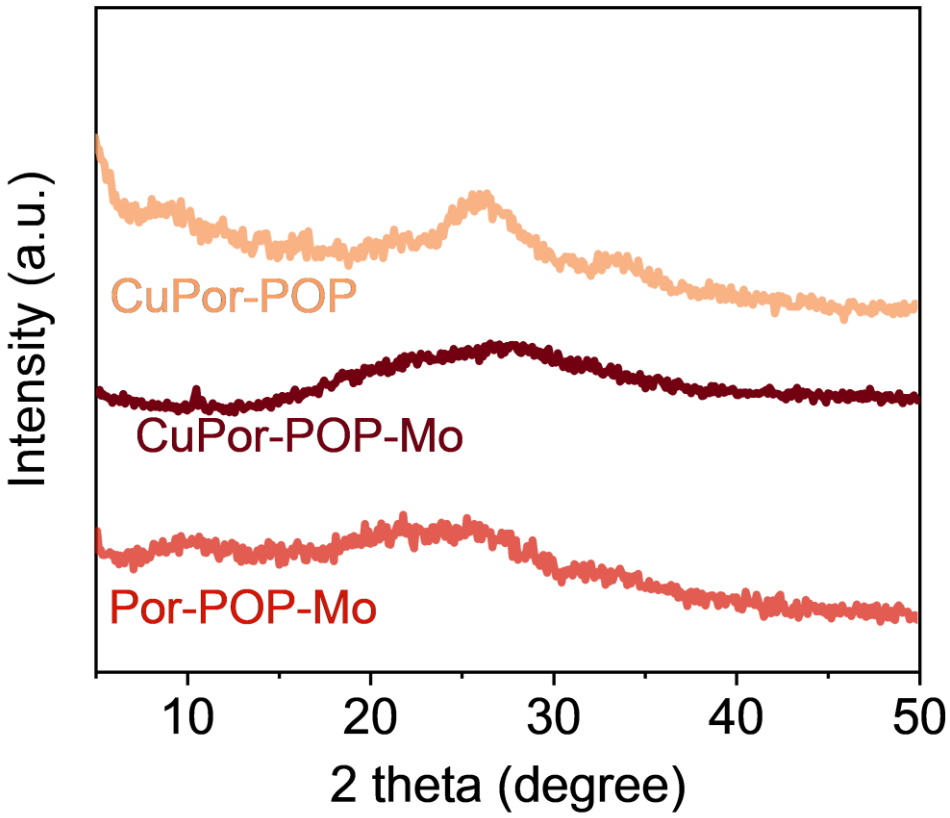

Supplementary Figure 3 PXRD. Powder XRD patterns of CuPor-POP, Por-POP-Mo and CuPor-POP-Mo.

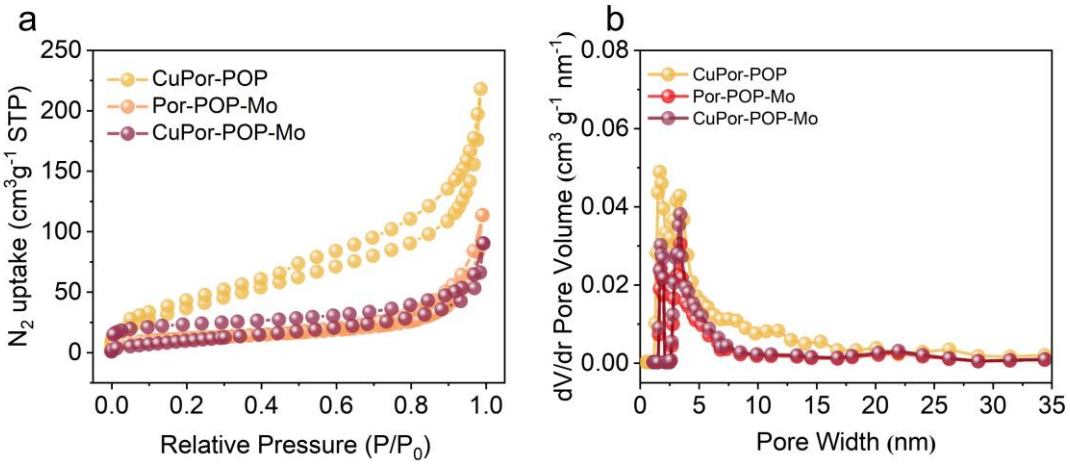

Supplementary Figure 4 Calculated non-local density functional theory (NLDFT) model for CuPor-POP, Por-POP-Mo, and CuPor-POP-Mo. a N_2 adsorption-desorption isotherms. **b** Pore size distribution.

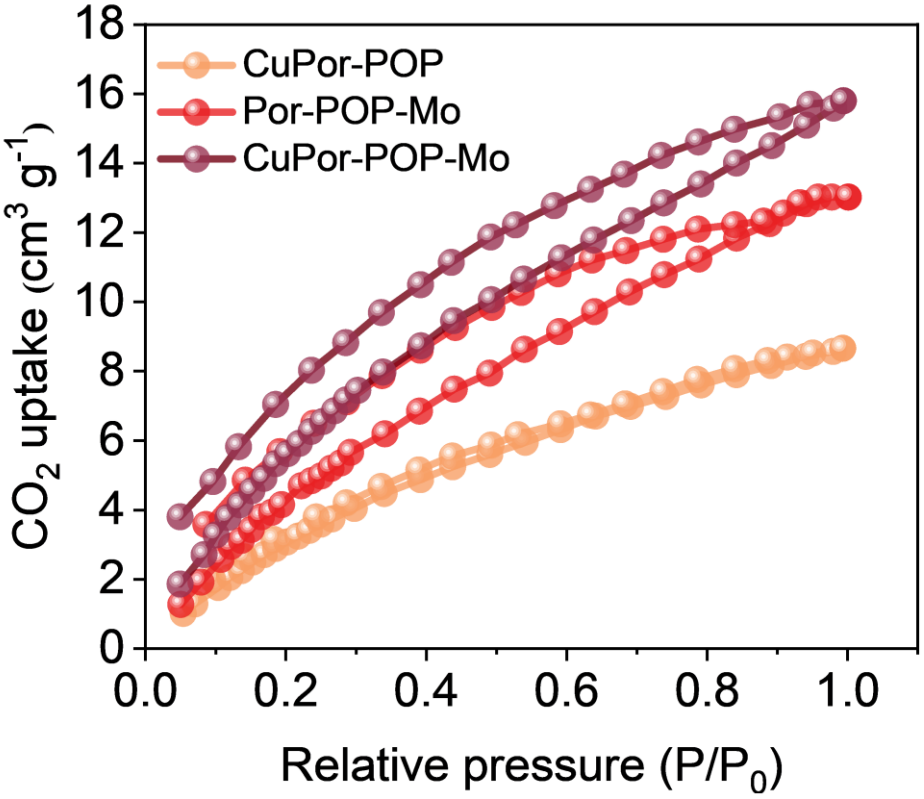

Supplementary Figure 5 CO_2 adsorption of all the POPs. CO_2 adsorption capacity of CuPor-POP, Por-POP-Mo, and CuPor-POP-Mo at 25 °C.

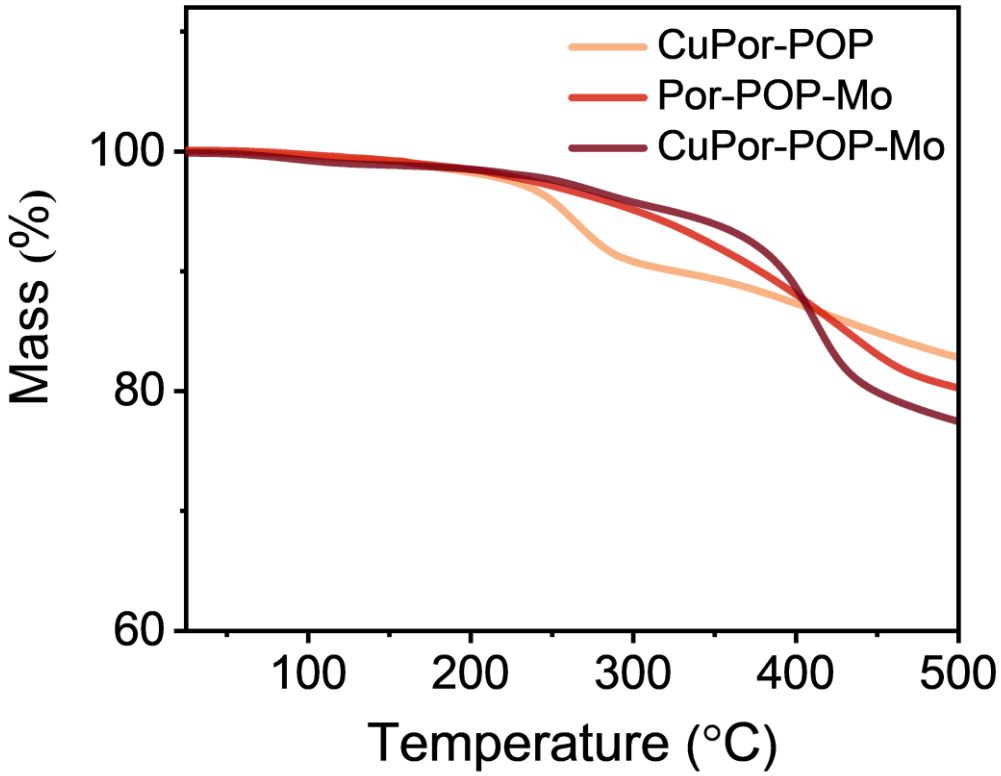

Supplementary Figure 6 TGA. TGA curves of all the samples under the Argon gas.

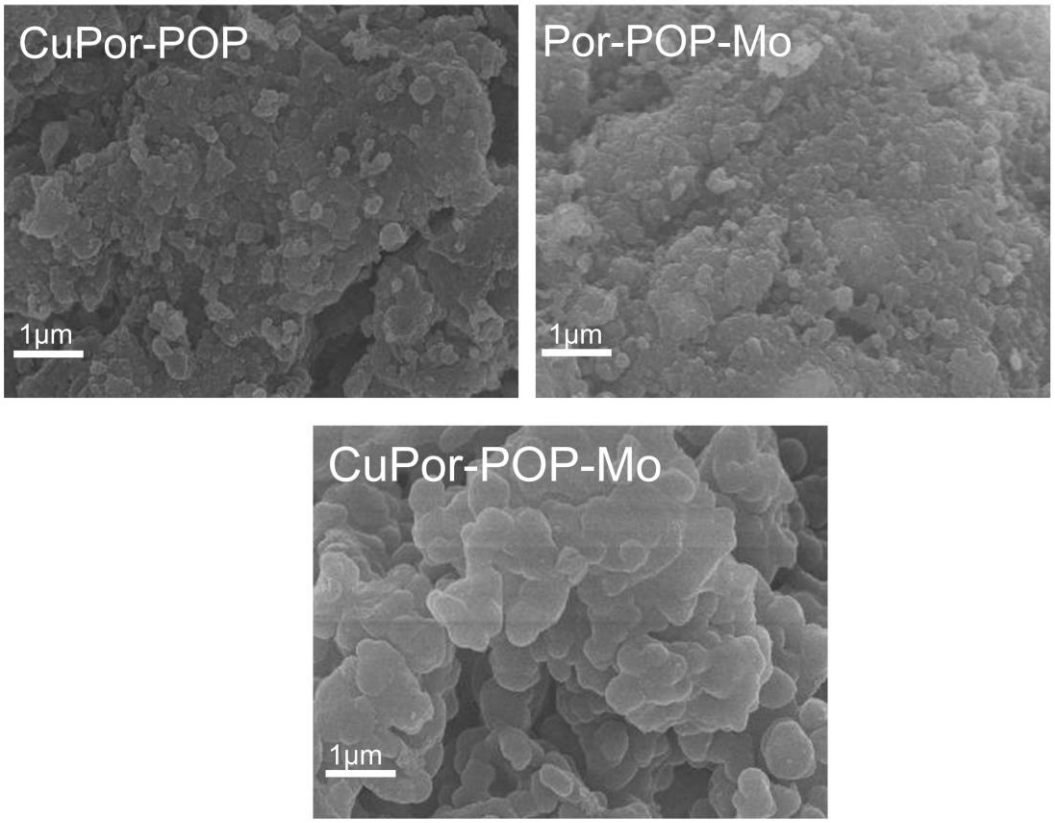

Supplementary Figure 7 SEM images. SEM images of CuPor-POP, Por-POP-Mo, and CuPor-POP-Mo.

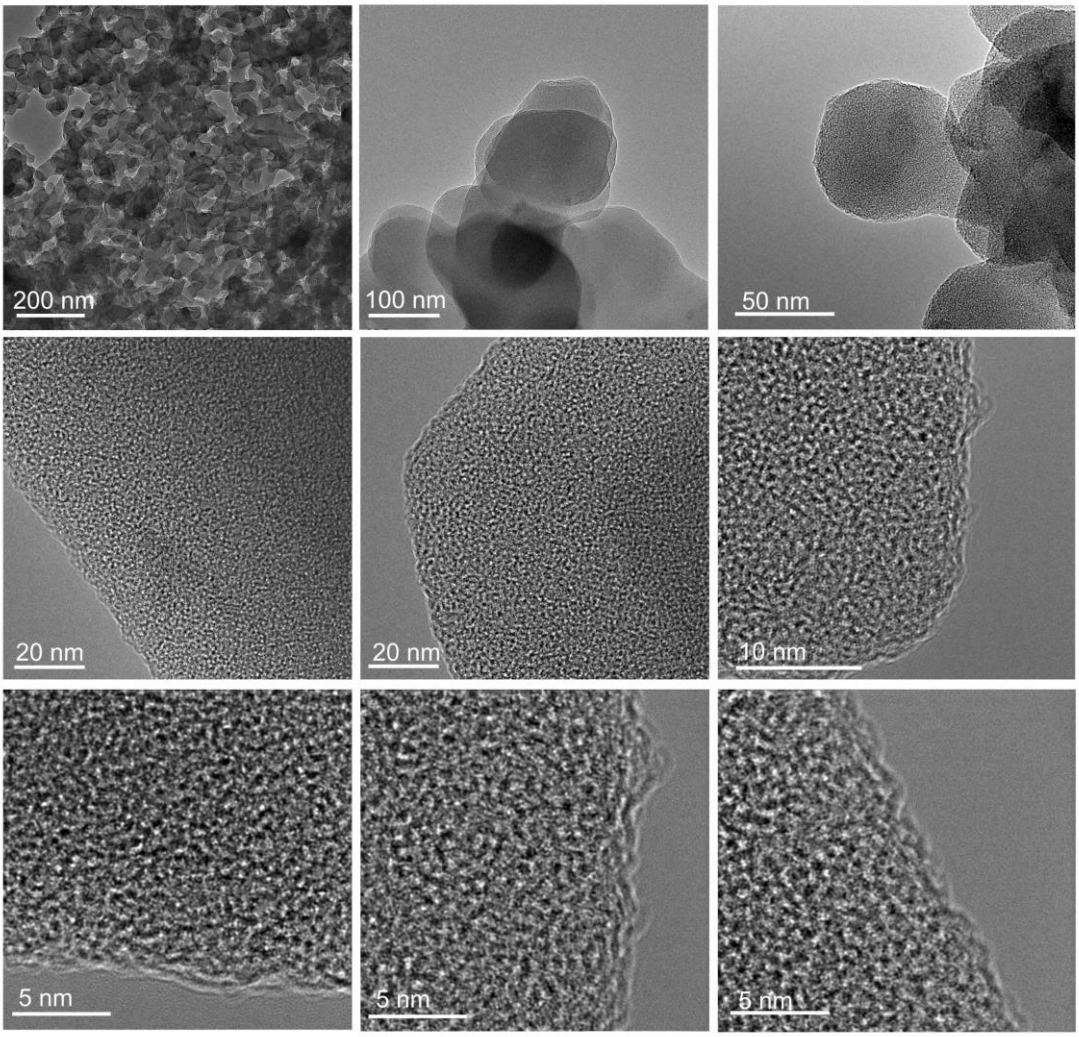

Supplementary Figure 8 TEM images. TEM images of CuPor-POP-Mo.

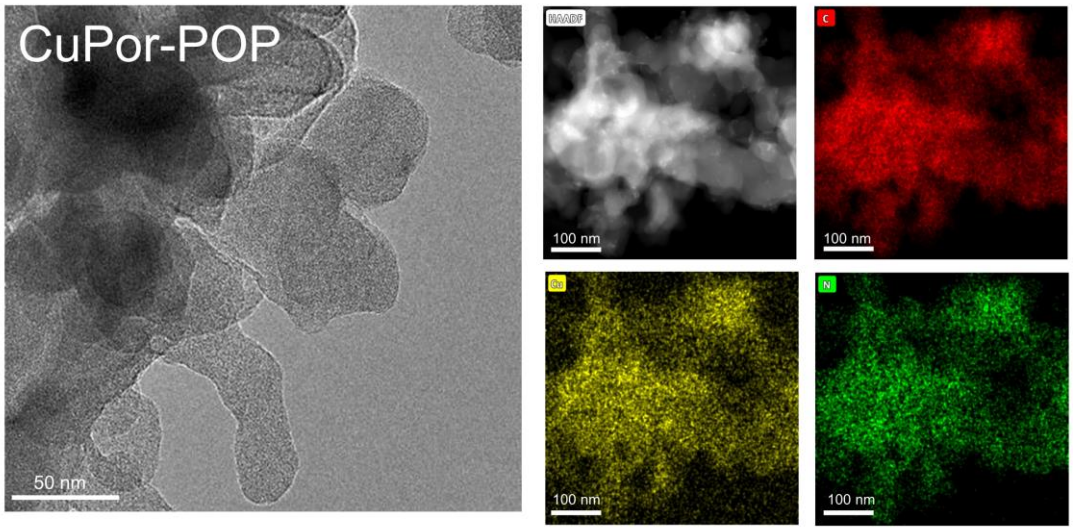

Supplementary Figure 9 TEM images and energy-dispersive X-ray spectrum (EDS) mapping of CuPor-POP. Carbon mapped in red, Nitrogen mapped in green and copper mapped in yellow.

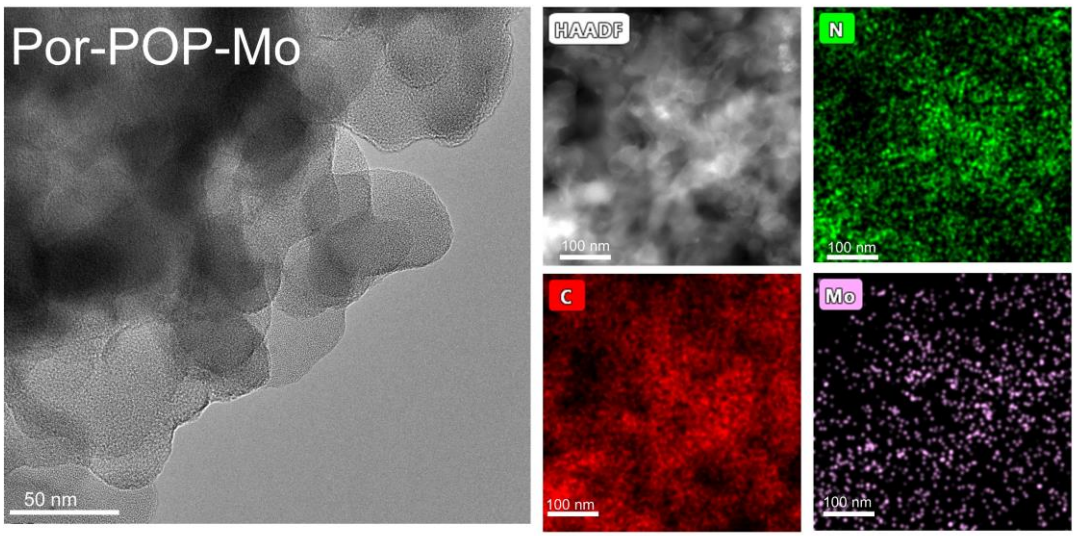

Supplementary Figure 10 TEM images and energy-dispersive X-ray spectrum (EDS) mapping of Por-POP-Mo. Nitrogen mapped in green, carbon mapped in red and molybdenum mapped in purple.

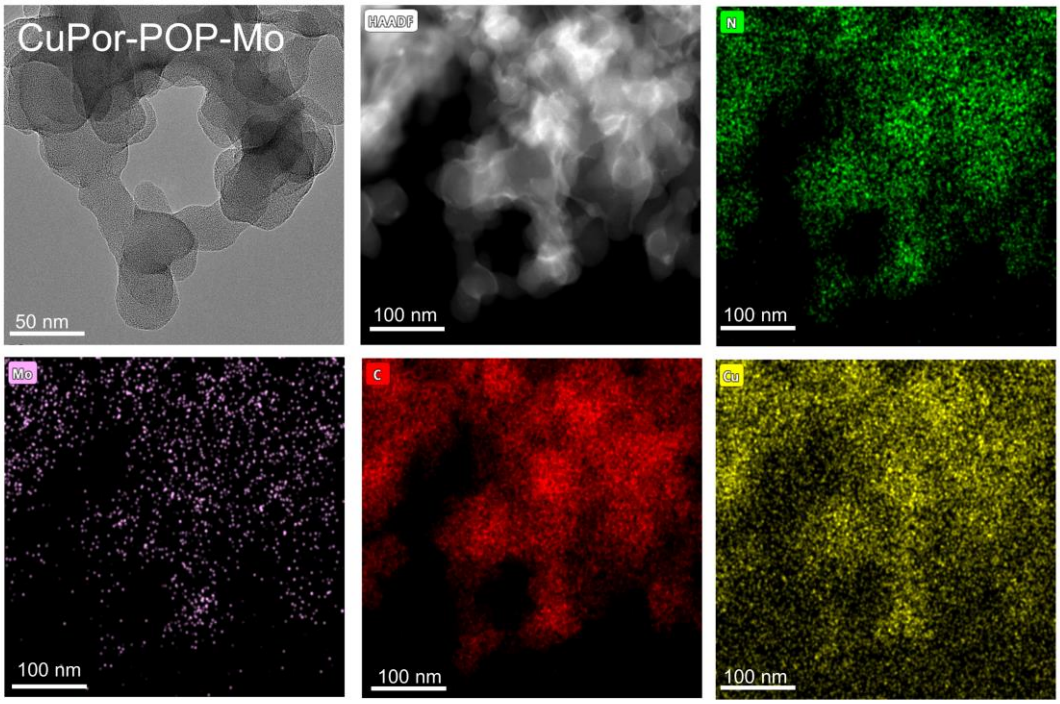

Supplementary Figure 11 TEM images and energy-dispersive X-ray spectrum (EDS) mapping of CuPor-POP-Mo. Nitrogen mapped in green, molybdenum mapped in purple, carbon mapped in red and copper mapped in yellow.

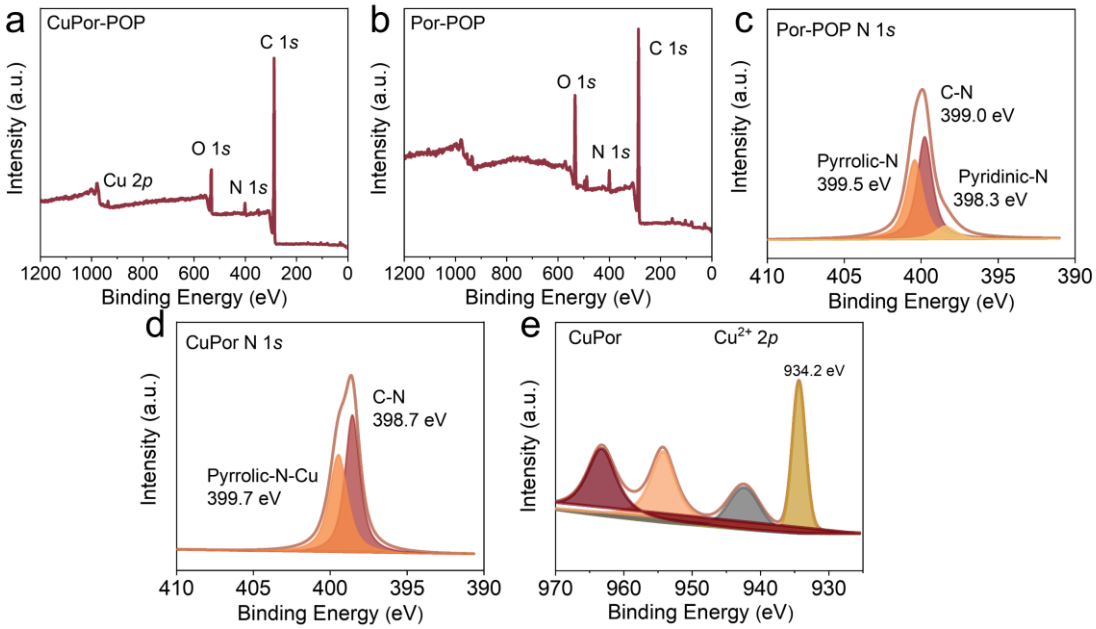

Supplementary Figure 12 XPS survey spectrum for CuPor-POP, Por-POP and CuPor. a-b XPS survey spectrum for CuPor-POP and Por-POP. **c** High-resolution XPS spectrum for N 1*s* of Por-POP. **d-e** High-resolution XPS spectrum for N 1*s* and Cu 2*p* of CuPor.

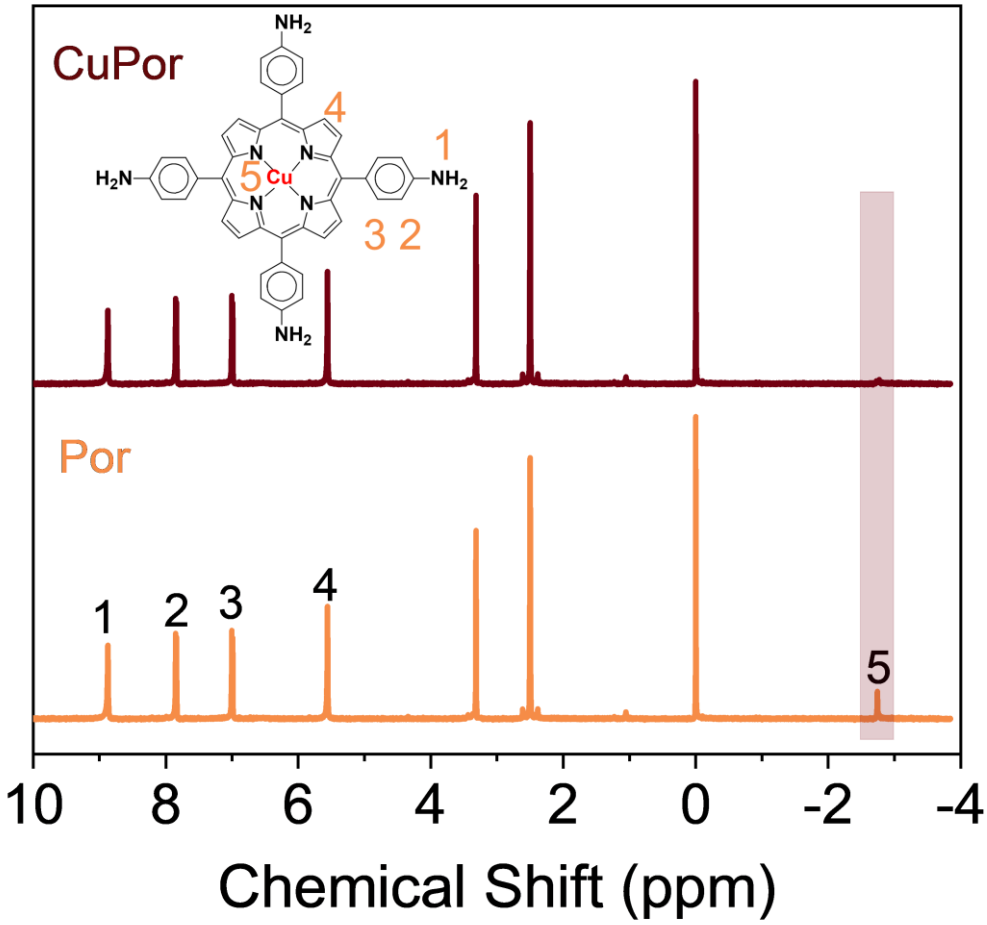

Supplementary Figure 13 ^{1}H NMR spectrum. ^{1}H NMR spectrum of Por and CuPor.

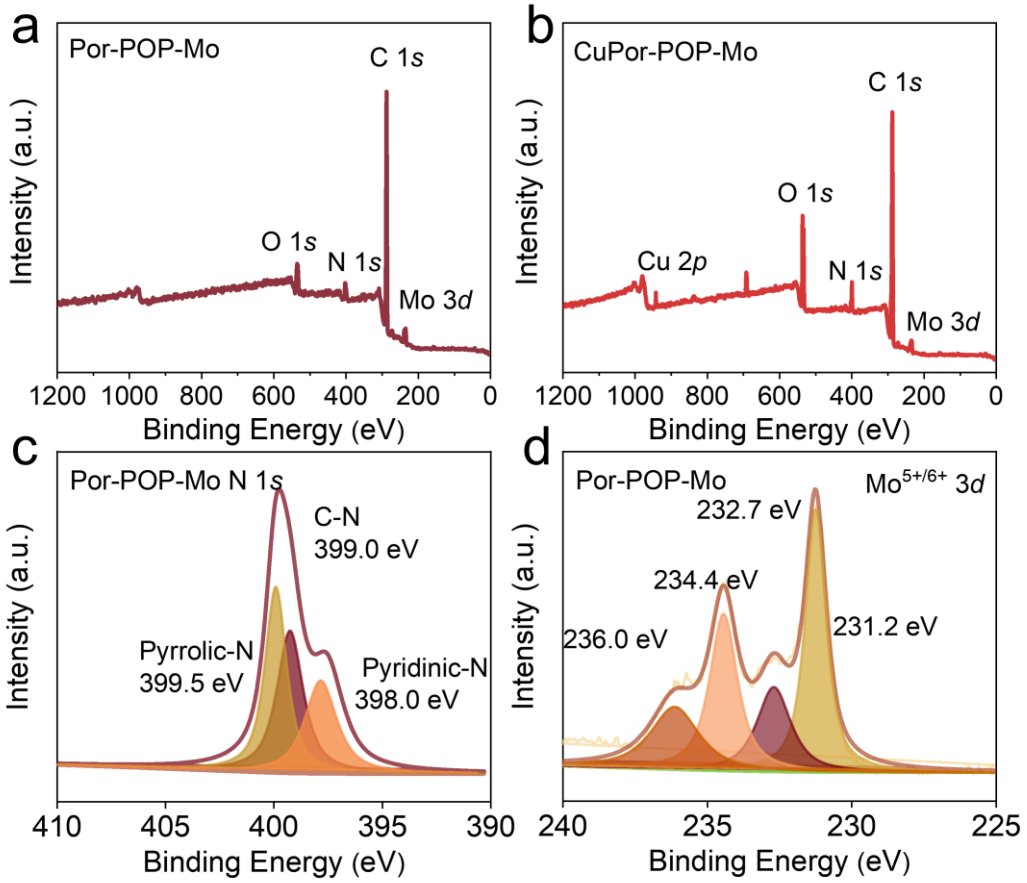

Supplementary Figure 14 XPS survey spectrum for Por-POP-Mo and CuPor-POP-Mo. a-b XPS survey spectrum for Por-POP-Mo and CuPor-POP-Mo. **c-d** High-resolution XPS spectrum c of N 1*s*, and d of Mo 3*d* for Por-POP-Mo.

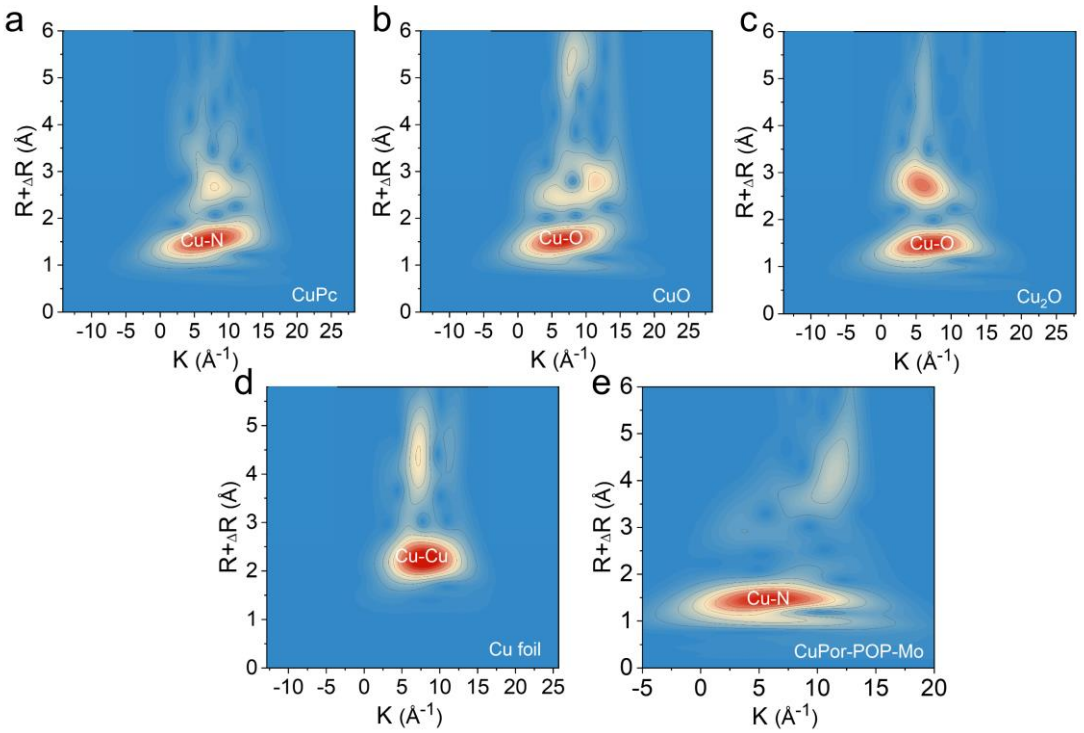

Supplementary Figure 15 WT-EXAFS spectrum in discriminating radial distance and k-space resolution of CuPor-POP-Mo. **a** CuPc. **b** CuO. **c** Cu_2O. **d** Cu foil. **e** CuPor-POP-Mo.

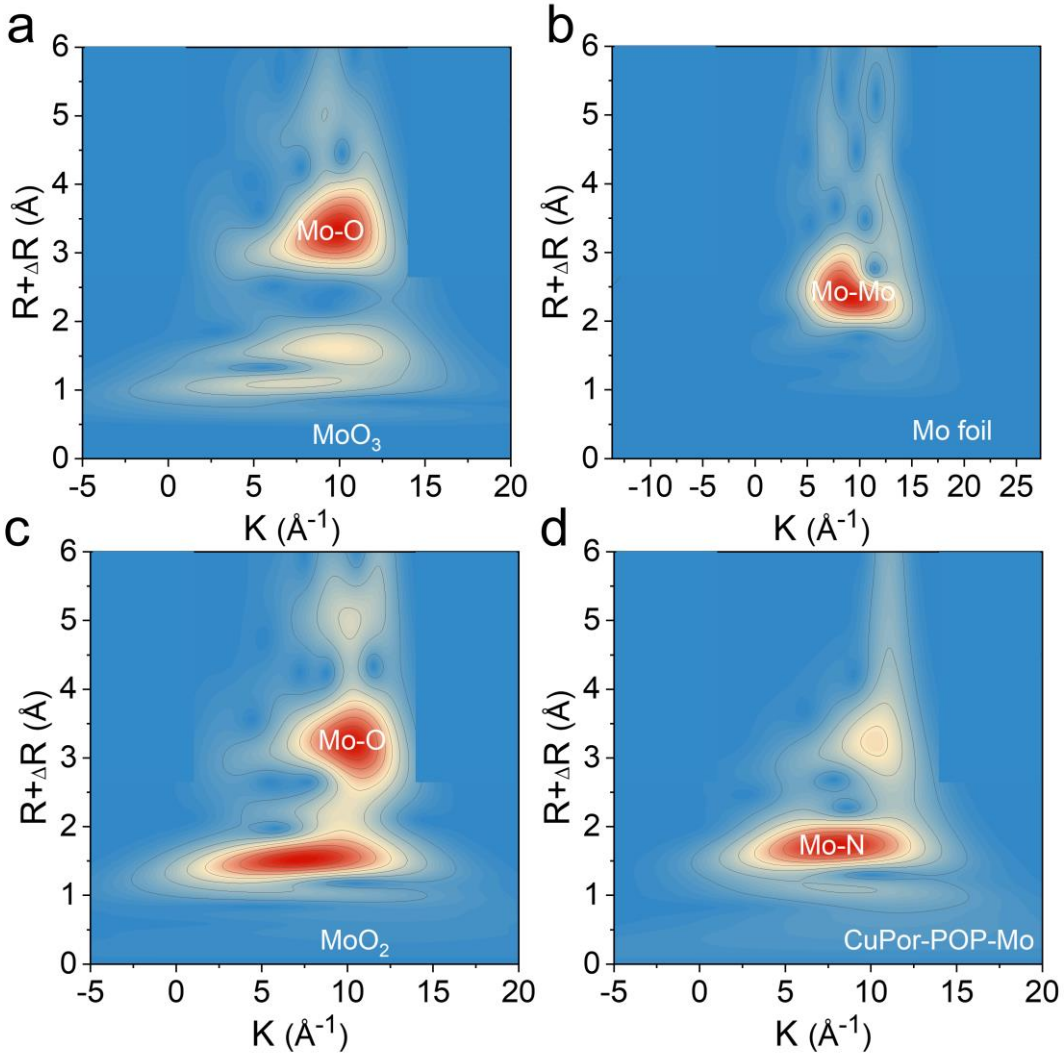

Supplementary Figure 16 WT-EXAFS spectra in discriminating radial distance and k-space resolution of the standard sample. a MoO_3. **b** Mo foil. **c** MoO_2. **d** CuPor-POP-Mo.

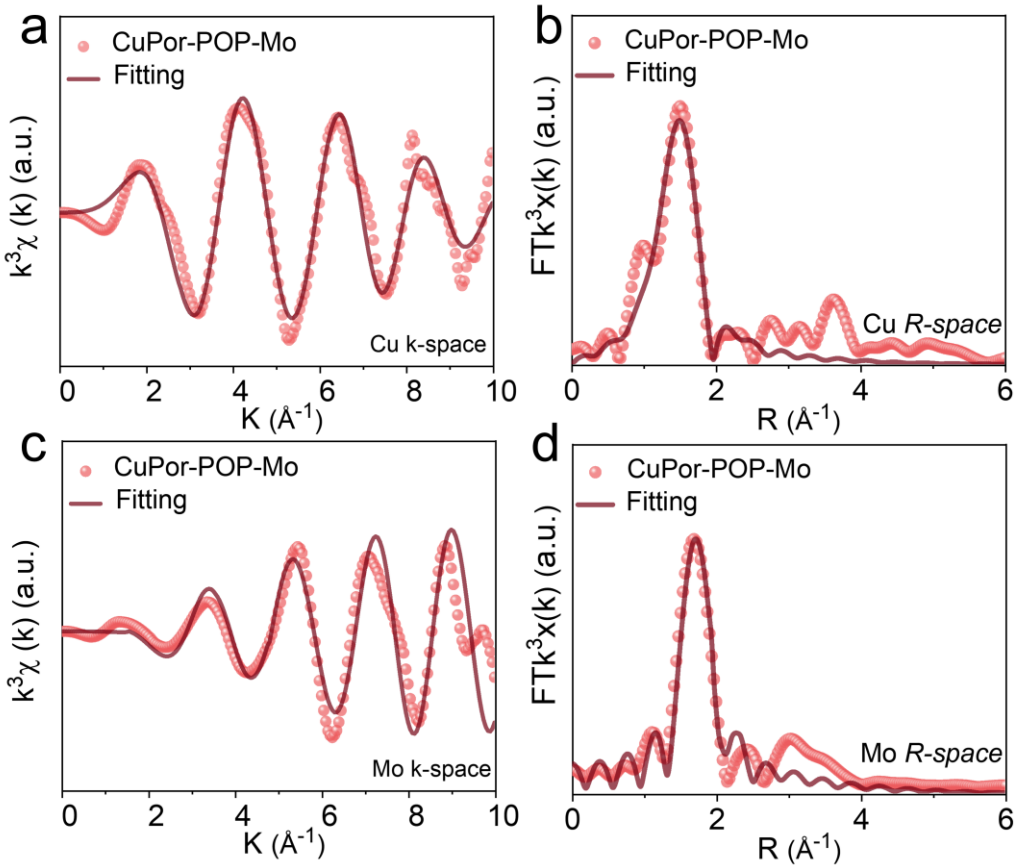

Supplementary Figure 17 EXFAS fitting curves for CuPor-POP-Mo. a in Cu k-space. **b** in Cu R-space. **c** in Mo k-space. **d** in Mo R-space.

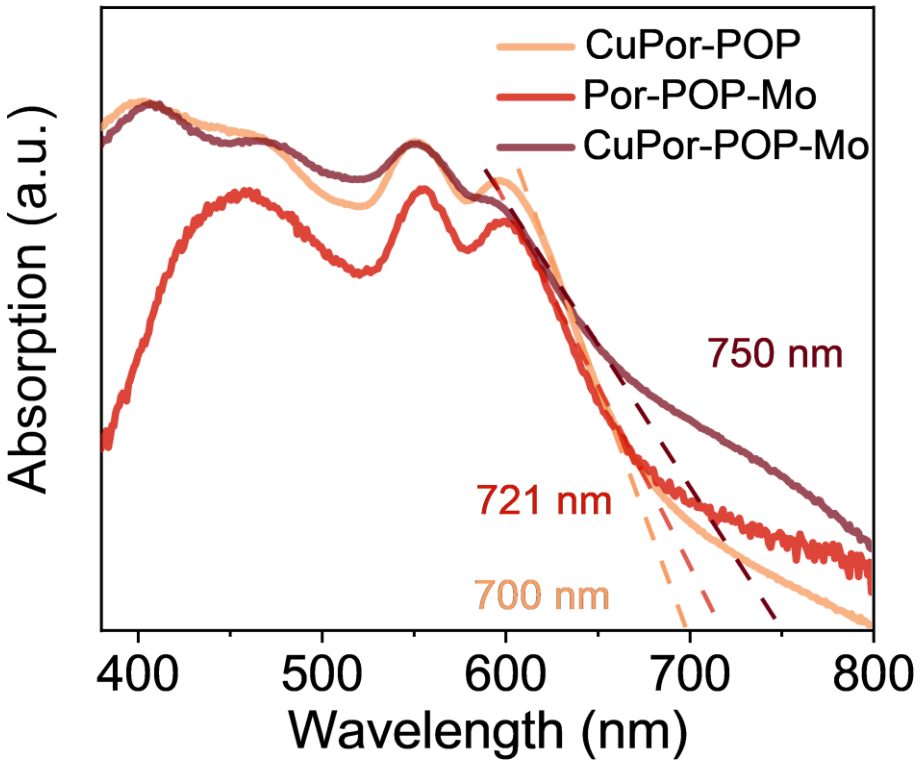

Supplementary Figure 18 Solid-state UV-vis diffuse reflectance spectra. Solid-state UV-vis diffuse reflectance spectra of CuPor-POP, Por-POP-Mo and CuPor-POP-Mo.

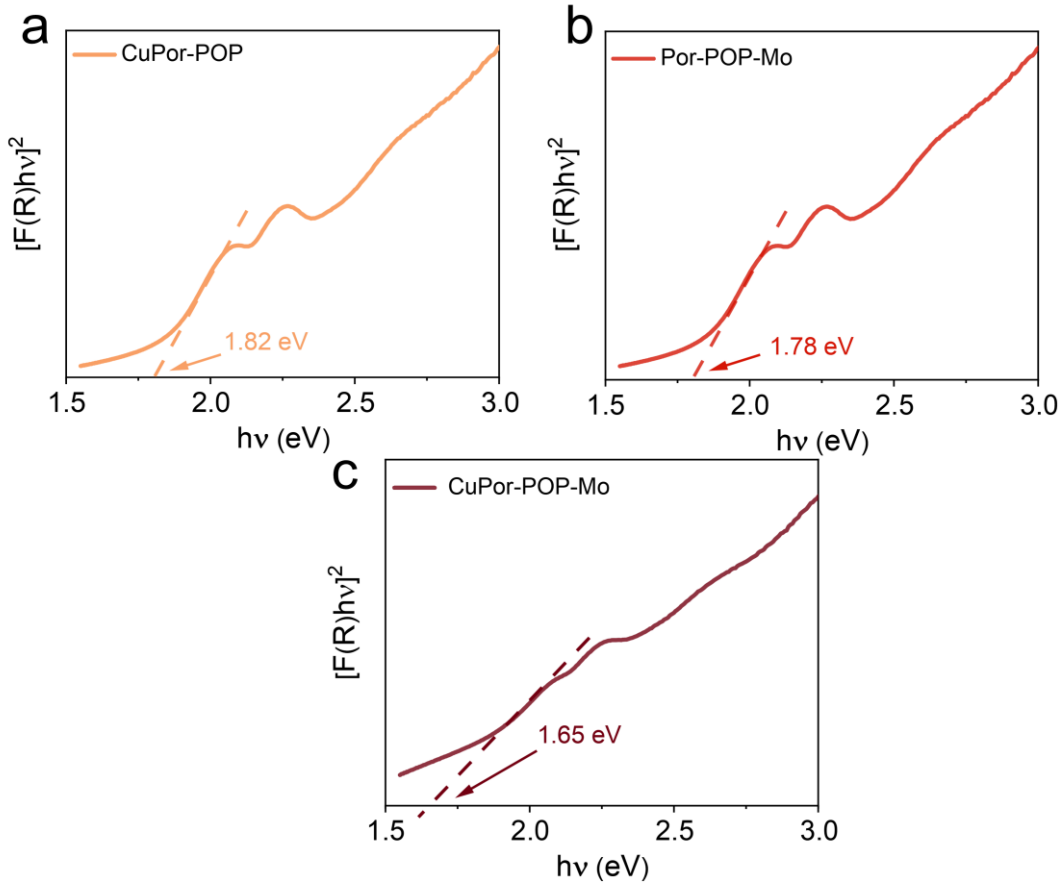

Supplementary Figure 19 Tauc plots of all the samples derived from solid-state UV-vis diffuse reflectance spectra in Supplementary Figure 18. a CuPor-POP. **b** Por-POP-Mo. **c** CuPor-POP-Mo.

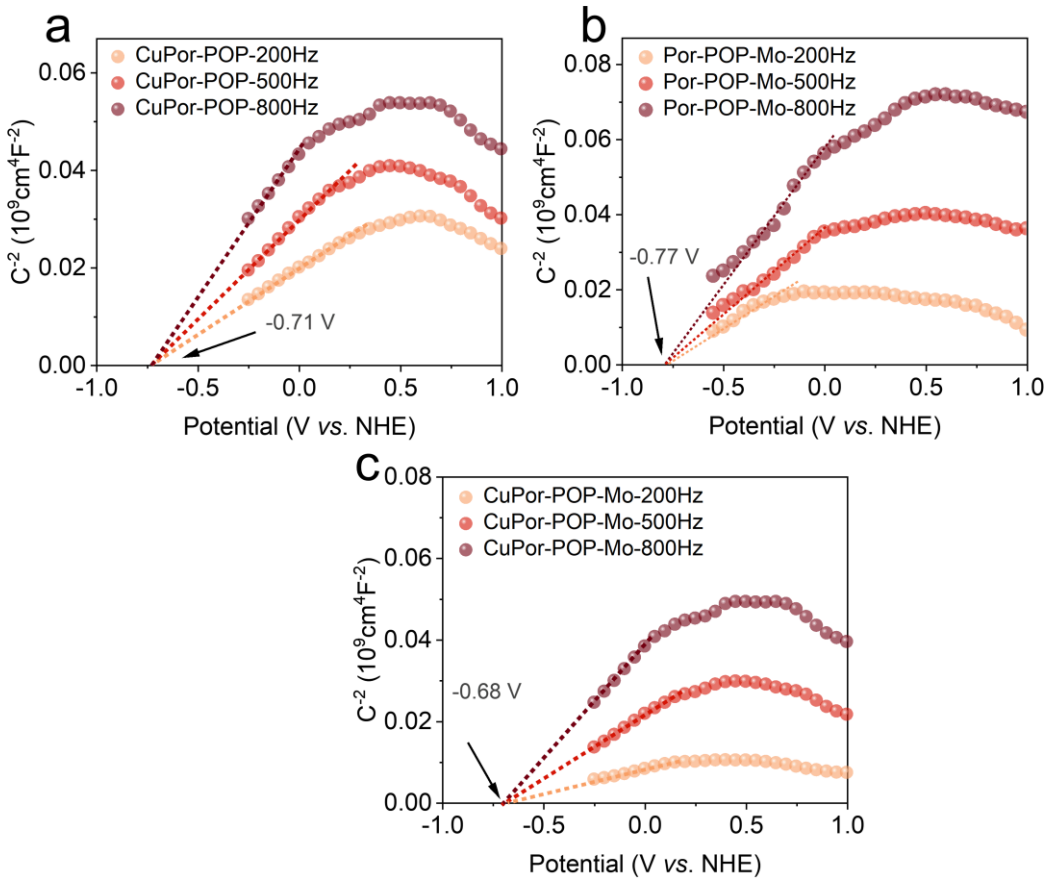

Supplementary Figure 20 Mott-Schottky plots at different frequencies (200, 500, and 800 Hz). a CuPor-POP. **b** Por-POP-Mo. **c** CuPor-POP-Mo.

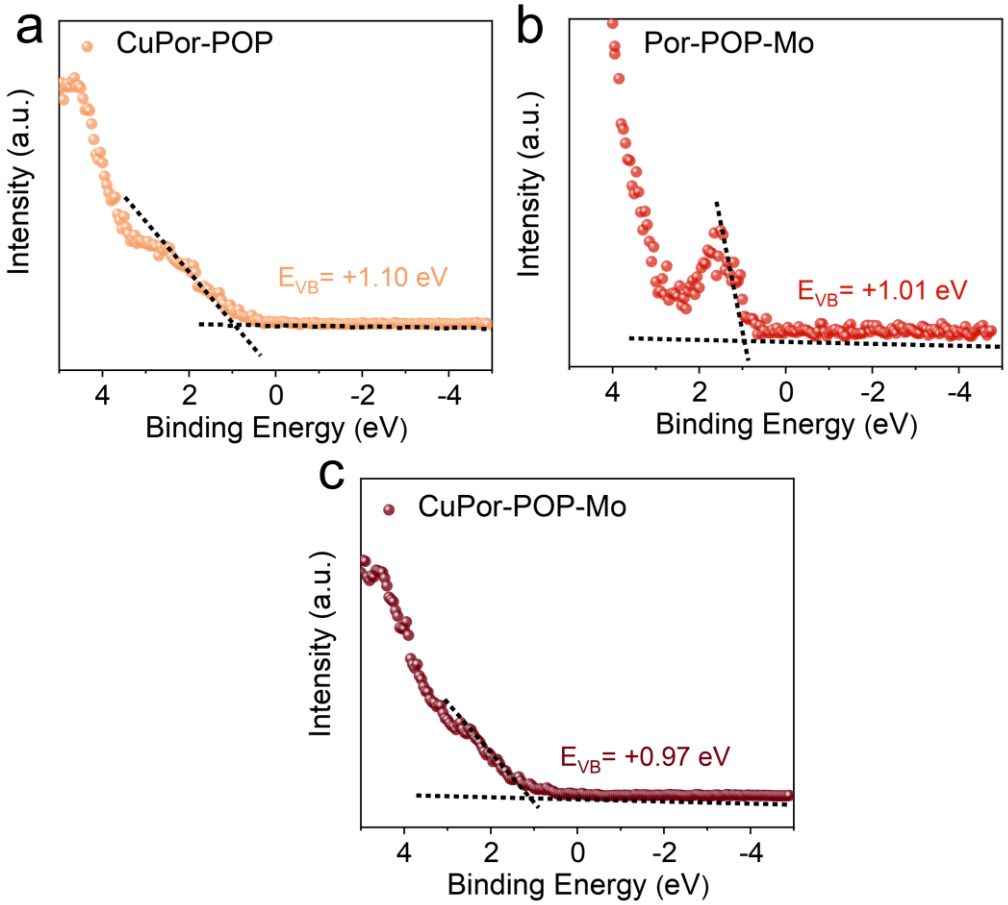

Supplementary Figure 21 XPS valance band spectra. a CuPor-POP. **b** Por-POP-Mo. **c** CuPor-POP-Mo.

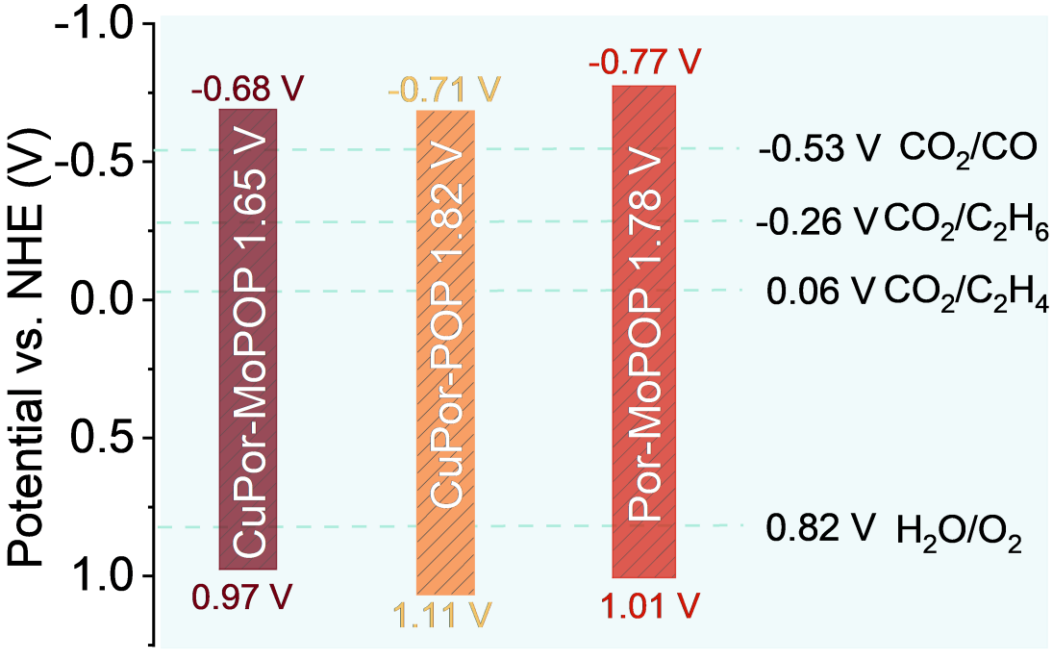

Supplementary Figure 22 Band structures. Band structures of CuPor-POP, Por-POP-Mo and CuPor-POP-Mo for CO_2 photoreduction.

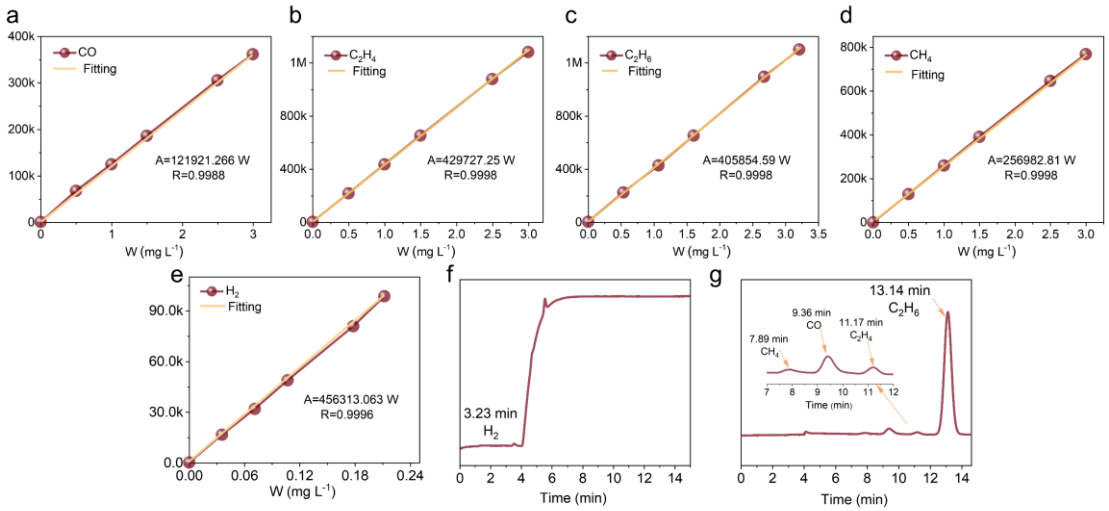

Supplementary Figure 23 GC analysis. Linear GC calibration plots **a** CO. **b** C_2H_4. **c** C_2H_6. **d** CH_4. **e** H_2. The corresponding retention time based on the GC profile of the CuPor-POP-Mo: f H_2 and **g** CO and hydrocarbon.

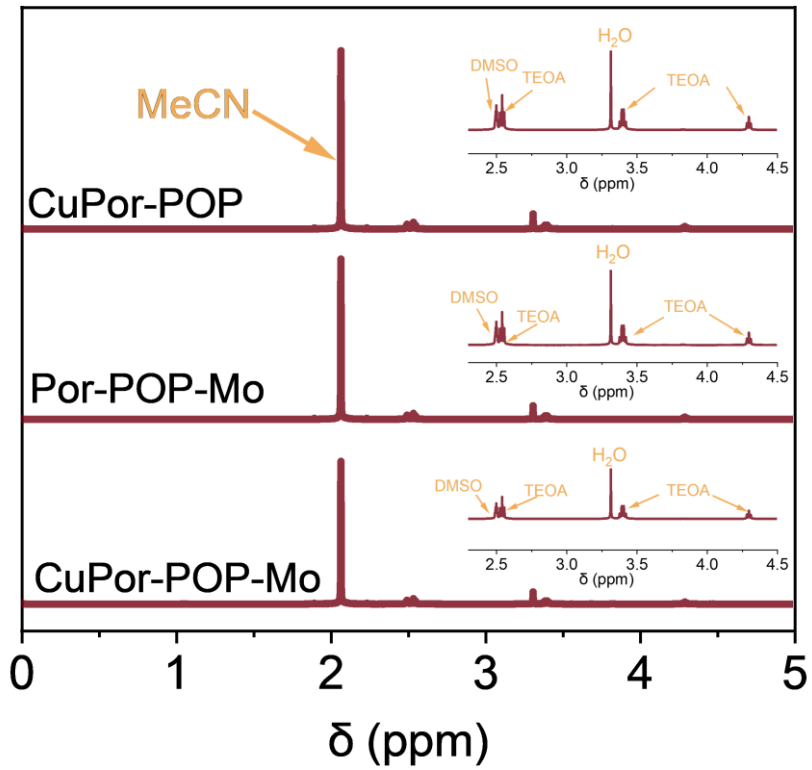

Supplementary Figure 24 ^{1}H-NMR spectra of POPs in the liquid products after 4 h. d^6-DMSO was used as the internal standard.

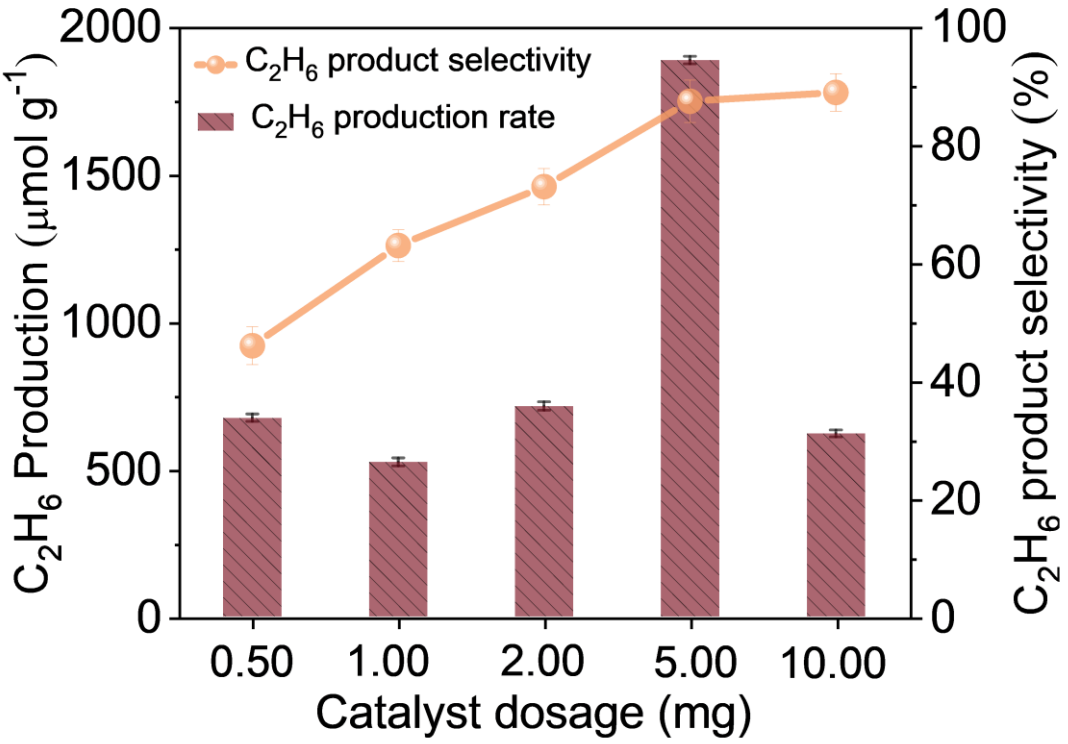

Supplementary Figure 25 Dependence of catalyst mass-loading on photocatalytic C_2H_6 production within 4 h. The error bars for C_2H_6 evolution uncertainty represent the standard deviation based on three independent measurements of each sample.

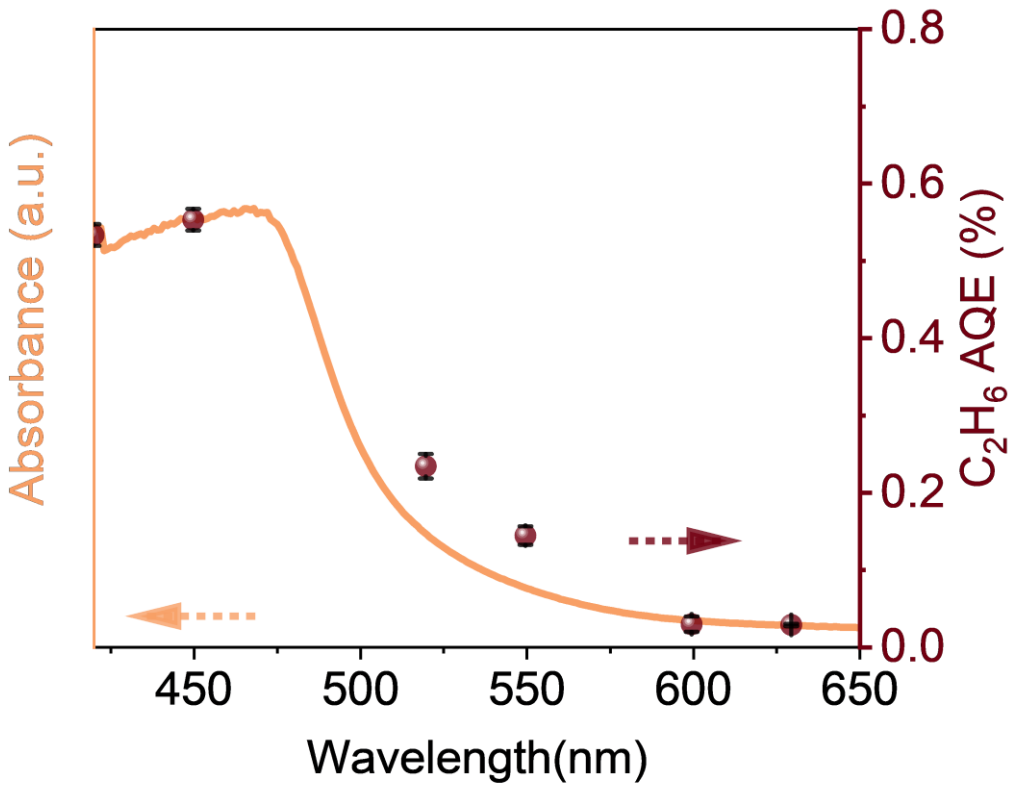

Supplementary Figure 26 AQE of C_2H_6 production catalyzed by CuPor-POP-Mo at different wavelengths and the related visible spectrum. The error bars for C_2H_6 evolution uncertainty represent the standard deviation based on three independent measurements of each sample.

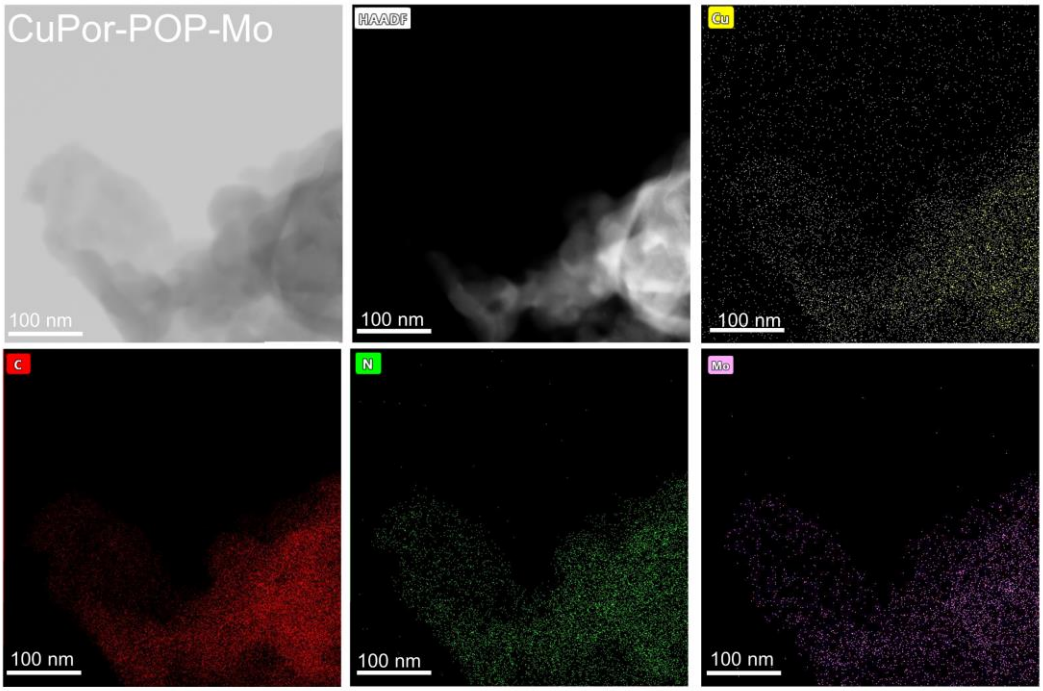

Supplementary Figure 27 TEM images and corresponding elemental mapping after photocatalysis. TEM images and corresponding elemental mapping of CuPor-POP-Mo after the 4th cycle of the photocatalytic tests.

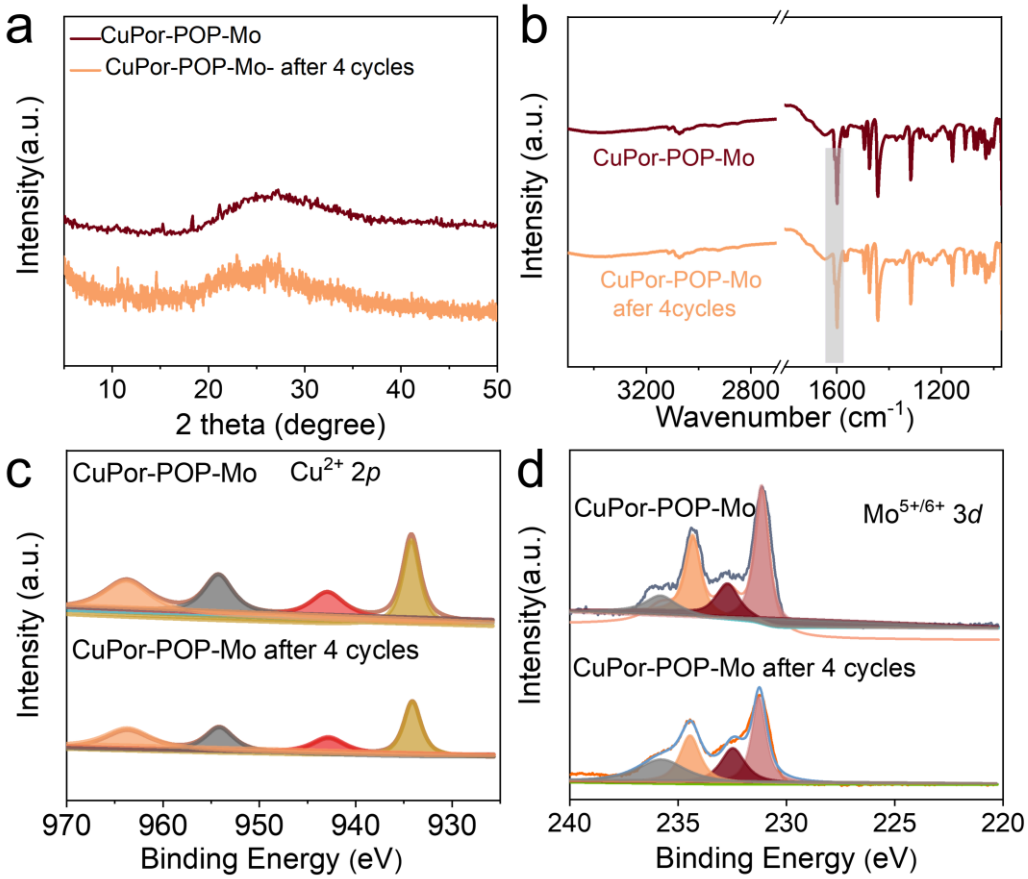

Supplementary Figure 28 Chemical stability of CuPor-POP-Mo before and after 4 cycles CO_2 photoreduction process. a XRD patterns. **b** FTIR spectra. **c-d** High-resolution XPS spectra of CuPor-POP-Mo before and after 4 cycles of the CO_2 photoreduction process.

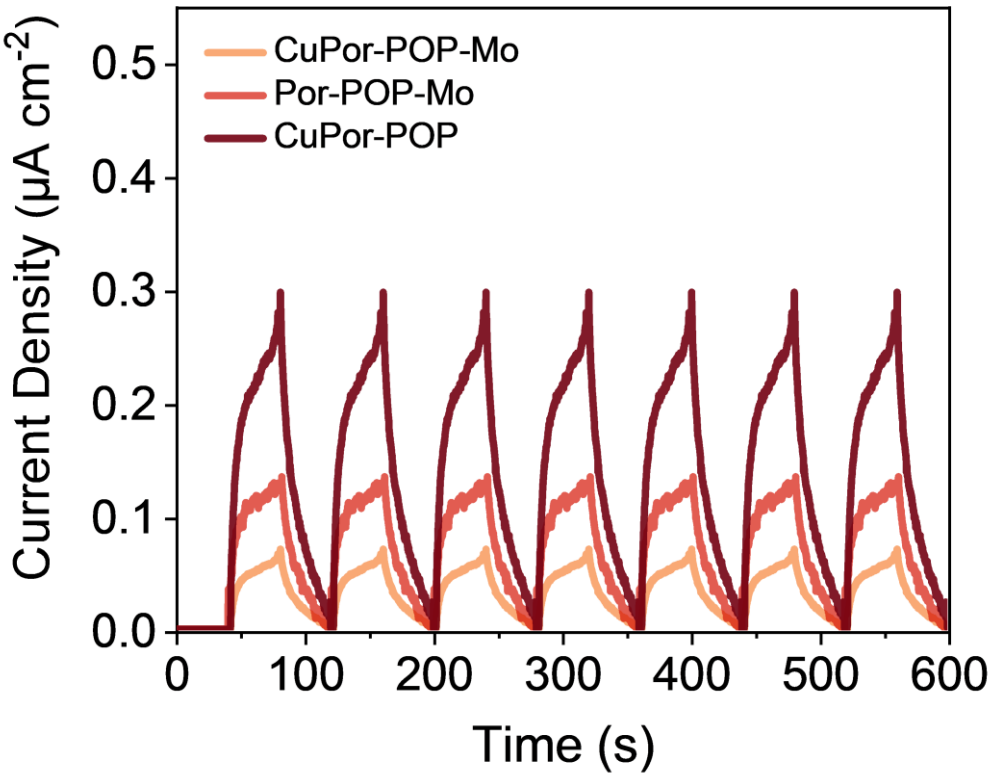

Supplementary Figure 29 Photoresponsive current density analyst. Transient photocurrent density under Xenon lamp (≥ 420 nm) irradiation for all the samples.

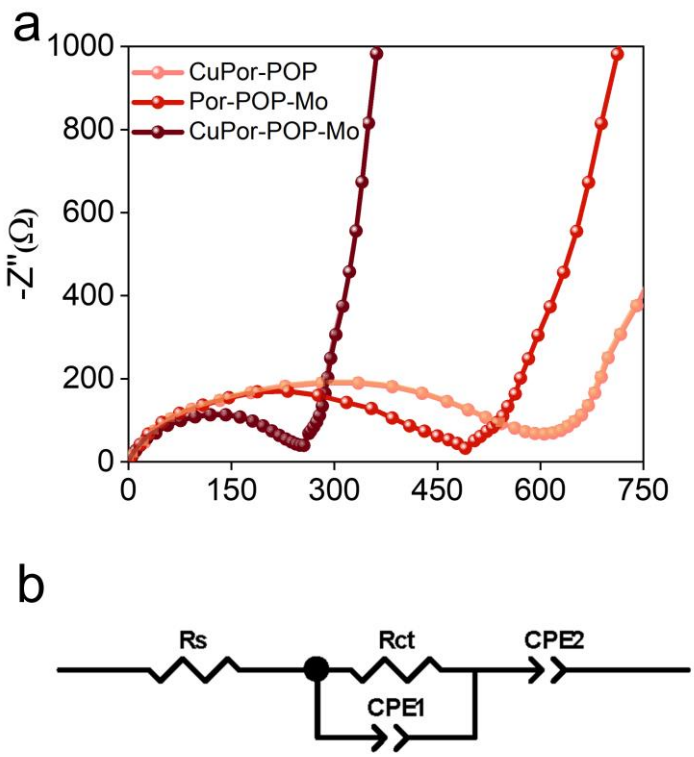

Supplementary Figure 30 Nyquist plots of all the samples based on electrochemical impedance spectroscopy (EIS) measurements. a CuPor-POP, Por-POP-Mo and CuPor-POP-Mo. **b** The related equivalent circuit.

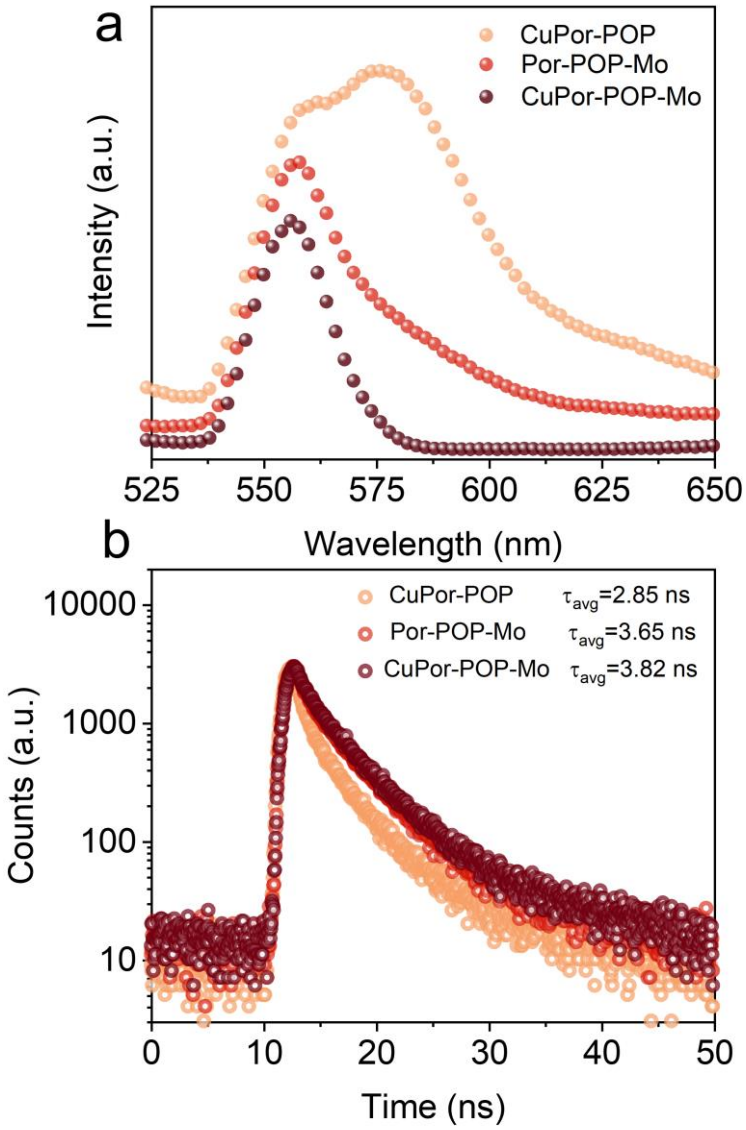

Supplementary Figure 31 Steady-state PL spectra and PL decay spectra of all samples. a Steady-state PL spectra of CuPor-POP, Por-POP-Mo and CuPor-POP-Mo. **b** PL decay spectra of CuPor-POP, Por-POP-Mo and CuPor-POP-Mo.

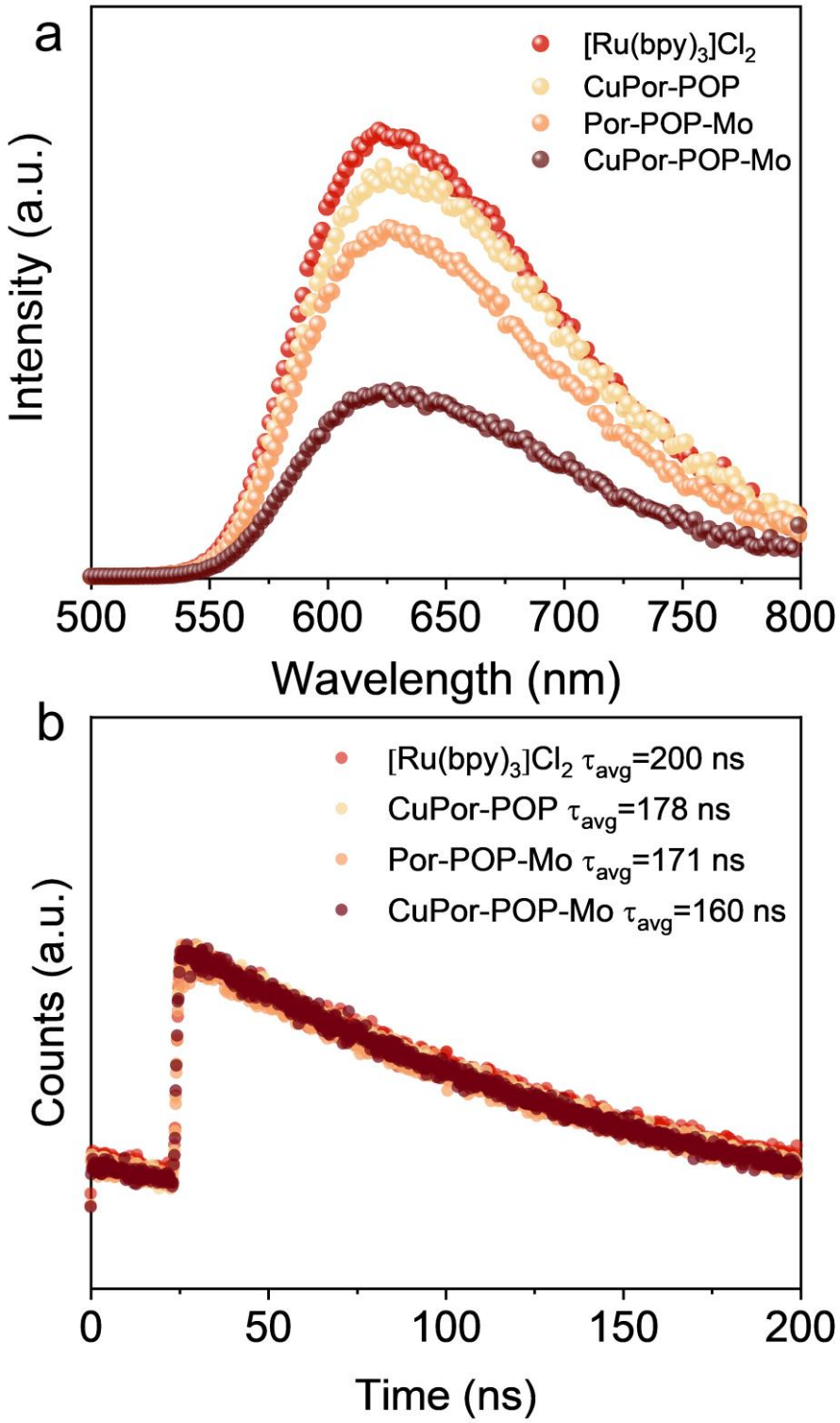

Supplementary Figure 32 Steady-state PL spectra and PL decay spectra of all sample in reaction system. a Steady-state PL spectra of $[Ru(bpy)_3]Cl_2$ (red), CuPor-POP+$[Ru(bpy)_3]Cl_2$ (yellow), Por-POP-Mo+$[Ru(bpy)_3]Cl_2$ (orange) and CuPor-POP-Mo+$[Ru(bpy)_3]Cl_2$ (dark red). **b** Steady-state PL decay spectra of $[Ru(bpy)_3]Cl_2$) with (CuPor-POP, Por-POP-Mo or CuPor-POP-Mo) and without catalyst (only $[Ru(bpy)_3]Cl_2$).

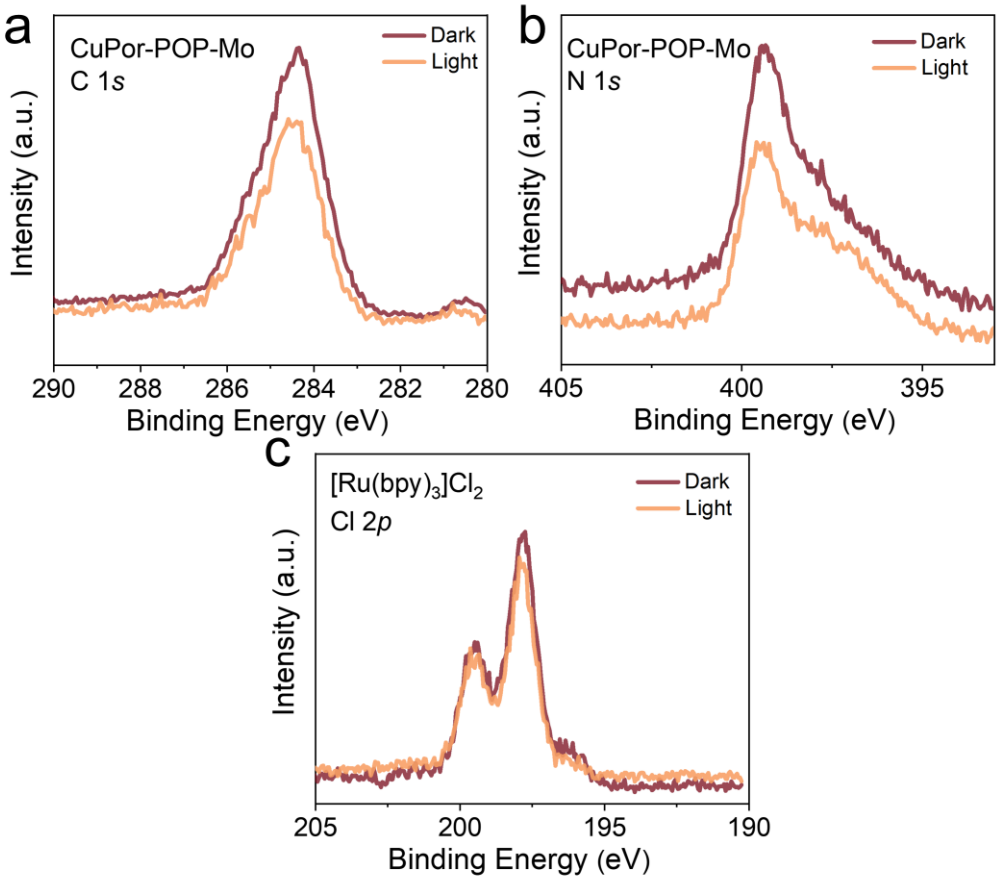

Supplementary Figure 33 Quasi-in situ XPS spectra. a C 1*s*, **b** N 1*s* and **c** Cl 2*p* before and after light irradiation.

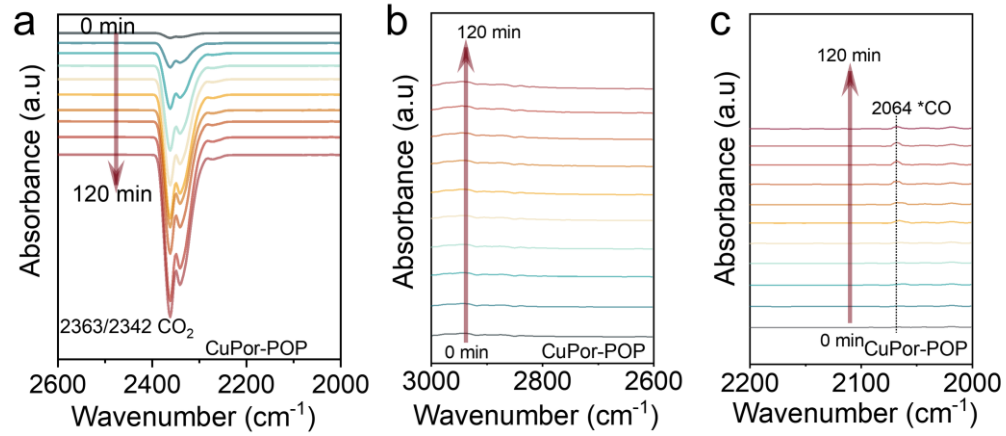

Supplementary Figure 34 In situ ATR-FTIR spectra. In situ ATR-FTIR spectra of CuPor-POP for the detection of intermediates during CO_2 photoreduction.

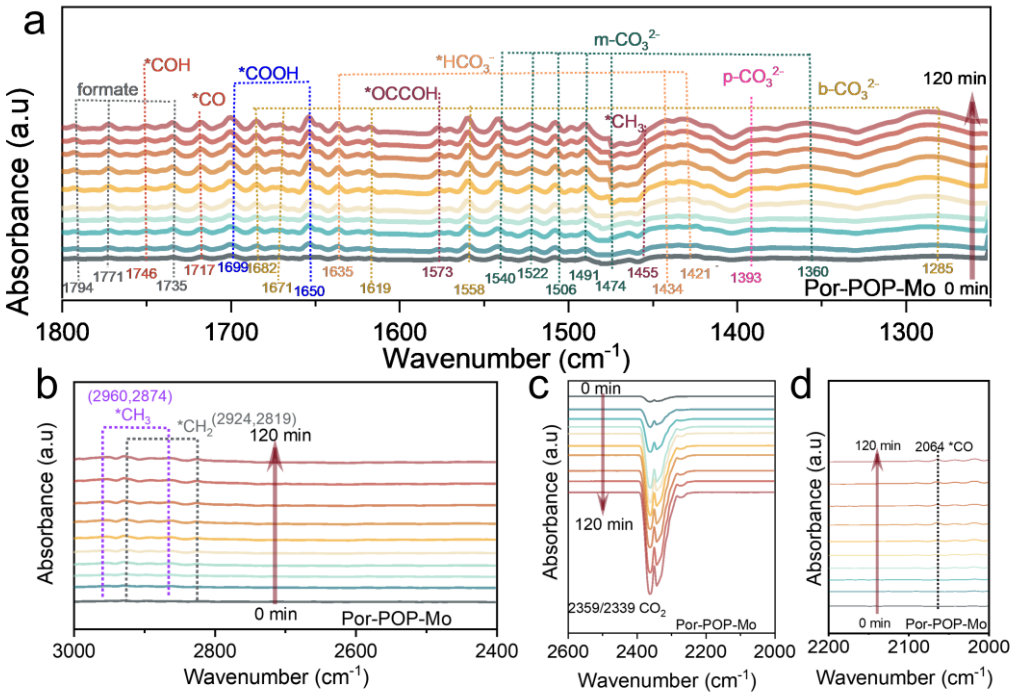

Supplementary Figure 35 In situ ATR-FTIR spectra. In situ ATR-FTIR spectra of Por-POP-Mo for the detection of intermediates during CO_2 photoreduction.

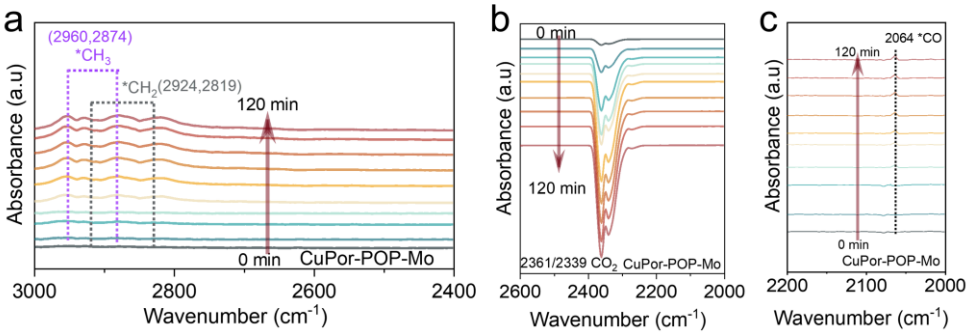

Supplementary Figure 36 In situ ATR-FTIR spectra. In situ ATR-FTIR spectra of CuPor-POP-Mo for the detection of intermediates during CO_2 photoreduction.

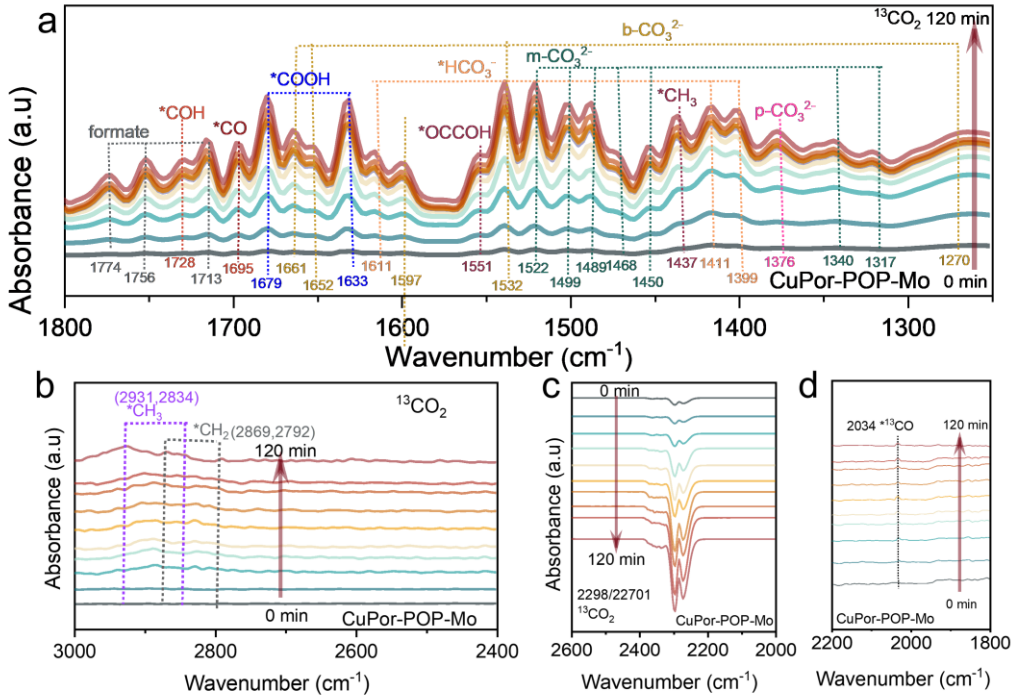

Supplementary Figure 37 In situ ATR-FTIR spectra. In situ ATR-FTIR spectra of CuPor-POP-Mo for the detection of intermediates during $^{13}CO_2$ photoreduction.

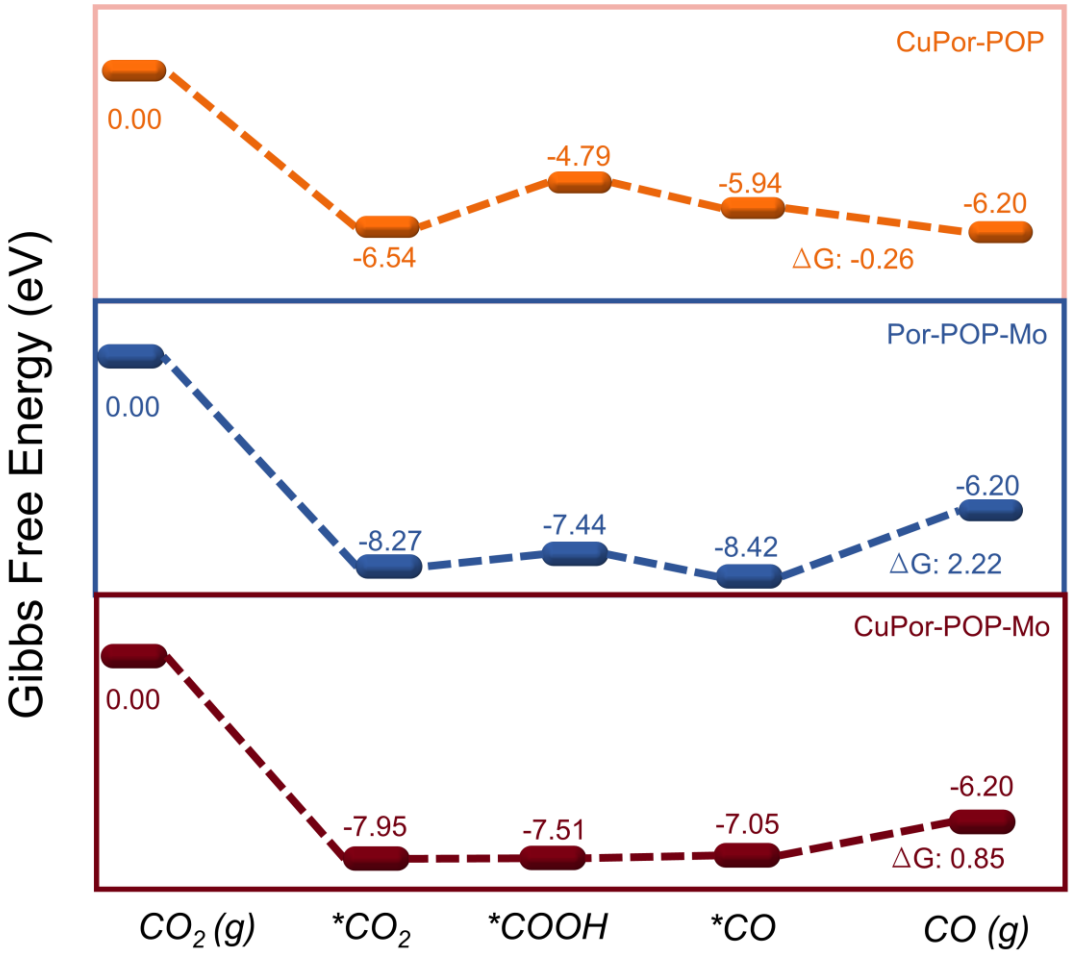

Supplementary Figure 38 The reaction Gibbs free energy change. Gibbs free energy profile of CuPor-POP, Por-POP-Mo and CuPor-POP-Mo.

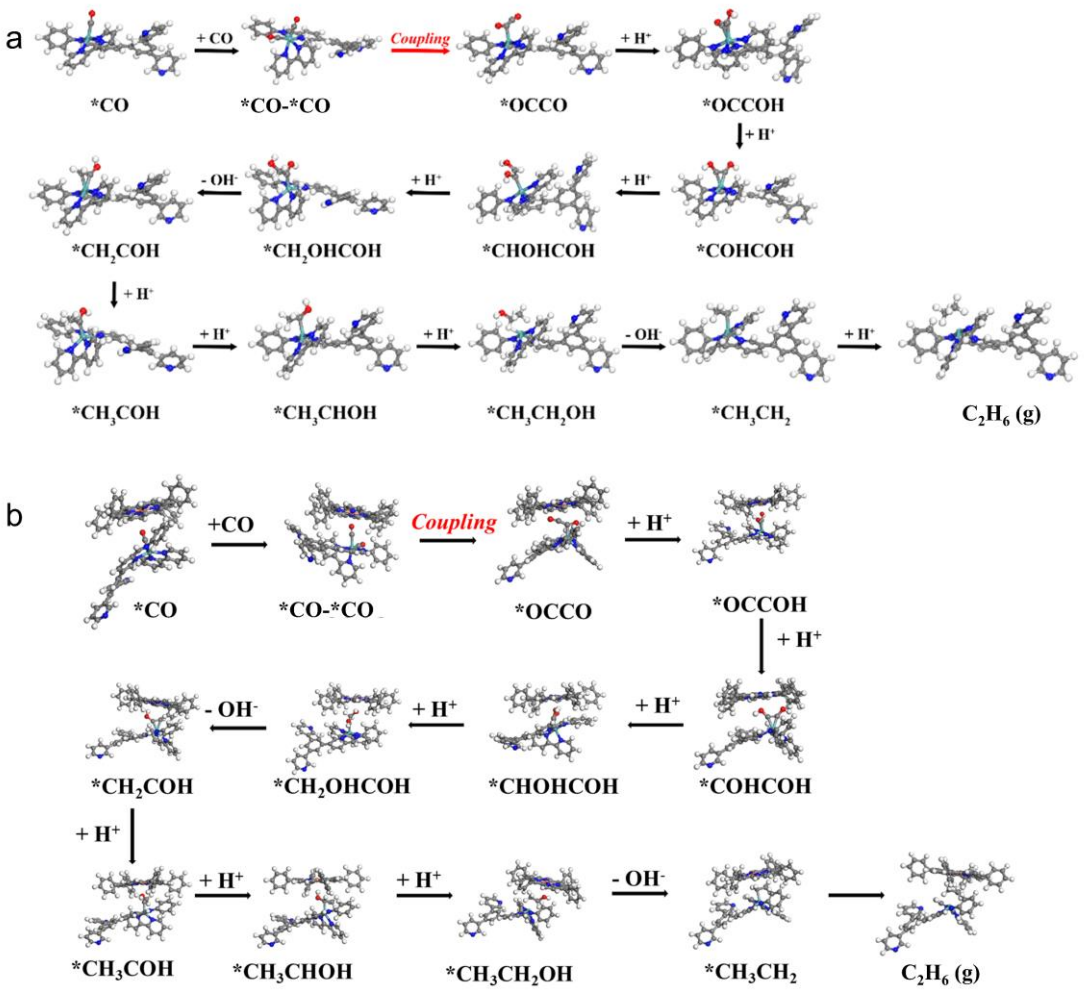

Supplementary Figure 39 The intermediates of C_2H_6 pathway. The intermediates of C_2H_6 pathway over **a** Por-POP-Mo and **b** CuPor-POP-Mo.

3. Supplementary Tables 1-5

Supplementary Table 1. EXAFS fitting results of CuPor-POP-Mo[a]

Sample	Shell	CN	R(Å)	σ^2(Å^2)	ΔE_0(eV)	*R factor*
CuPor-POP-Mo	Cu-N	4	2.02 ± 0.01	0.009 ± 0.002	1.25 ± 1.74	0.018
CuPor-POP-Mo	Mo-N	4	2.12 ± 0.01	0.012 ± 0.003	5.67 ± 2.25	0.019

[a] CN = coordination number, R = interatomic distance (the bond length between central atoms and surrounding coordination atoms) based on fitting results, ΔE_0 = inner potential correction, σ^2 = Debye-Waller factor, and the R factor is used to value the goodness of fit. Fourier transformed $k_2\chi(k)$ in the R-space using the ARTEMIS module of IFEFFIT S_0^2=0.912 for Cu and S_0^2=0.1 for Mo.

Supplementary Table 2. The content of each element in CuPor-POP-Mo determined from XPS

CuPor-POP-Mo	C	N	Cu	Mo
Atom (%)	92.95	5.71	0.56	0.78

Supplementary Table 3. Performance comparison of CO_2RR to C_2H_6 catalyzed by various photocatalysts

Photocatalyst	Catalytic condition	Light	Product	Production rate for C_2H_6 (μmol g^{-1} h^{-1})	C_2H_6 selectivity	Reference
CuPor-POP-Mo	TEOA, MeCN, H_2O, $[Ru(bpy)_3]Cl_2$ $6H_2O$	300 W Xe lamp (420-780 nm) 300 $mWcm^{-2}$	H_2, CO C_2H_4 C_2H_6	472.5	87.4%	This work
Cu SAs/CNP	TEOA, H_2O	300 W Xe lamp (Full spectrum)	CO,CH_4 C_2H_6	616.6	33%	[9]
Au_1/RP	$KHCO_3$+HCl, H_2O	300 W Xe lamp (Full spectrum)	CO,CH_4 C_2H_6	1.32	96%	[3]
$Ba_2Bi_{1.4}Ta_{0.6}O_5S$	H_2O	300 W Xe lamp (Full spectrum)	C_2H_6	5.4	30.2	[10]
Au/ZnO NSs	H_2O	300 W Xe lamp (Full spectrum), light intensity 595 mW)	CO,CH_4 C_2H_6	27	36	[11]
0.7Au/$ZnSn(OH)_6$	H_2O	300 W Xe lamp (Full spectrum)	CO, H_2 CH_4, C_2H_6	0.7	21	[12]
MoS_2@COF	TEOA, MeCN, H_2O, $[Ru(bpy)_3]Cl_2$ $6H_2O$	300 W Xe lamp (420-780 nm)	CO,CH_4 C_2H_4, C_2H_6	56.2	83.8	[13]
Cu-CuTCPP/g-C_3N_4	TEA, H_2O	300 W Xe lamp (360-800 nm)	CO,CH_4 C_2H_6	18.5	44	[14]
$Cu_{1.00\%}$–$Pt_{0.35\%}$–BT	H_2O	300 W Xe lamp (>400 nm)	CH_4 C_2H_6	25	4.7	[15]
Au@$Bi_{12}O_{17}Br_2$-700	H_2O	300 W Xe lamp (Full spectrum)	CO,CH_4 C_2H_6	29.3	65	[16]
Pt1/ZnNiTi-LDHs-E	H_2O, 0.2MPa	300 W Xe lamp (380-800 nm) 500 $mWcm^{-2}$	CO,CH_4 C_2H_6	29.8	20.5	[17]
Au@TiOx-Co(650)	H_2O	300 W Xe lamp (Full spectrum)	CO,H_2, CH_4 C_2H_6	58.7	25	[18]
Au-CeO_2	H_2O	300 W Xe lamp (Full spectrum) 394 $mWcm^{-2}$	CO, C_2H_6	11.1	65.3	[19]
CoAl/Ni1CuNP	TEOA, H_2O	300 W Xe lamp (>420 nm)	CO,CH_4 C_2H_6	25.3	27.4	[20]
$CABB_{20}$/UiO-66	ethyl acetate, H_2O,TEA	300 W Xe lamp (>420 nm) 230 $mWcm^{-2}$	CO,CH_4 C_2H_6	1.3	8.8	[21]
$NiSe_2$/g-C_3N_4	NaOH solution	300 W Xe lamp (Full spectrum) 415 $mWcm^{-2}$	CO, C_2H_6	46.1	97.5	[22]

Supplementary Table 4. Apparent quantum efficiency (AQE) of CuPor-POP-Mo at different wavelengths

Wavelengths (nm)	Intensity (mW cm^{-2})	AQE (%)
420	15.6	0.530
450	16.0	0.550
520	18.0	0.230
550	19.2	0.140
600	21.3	0.027
630	22.1	0.026

Supplementary Table 5. Average temperature, sunlight intensity and production rate of C_2H_6 during the outdoor tests for photocatalytic CO_2 reduction to C_2H_6

Day	Temperature (°C)	Light intensity (mW cm^{-2})	Production rate of C_2H_6 (μmol g^{-1} h^{-1})
1	26	51.2	283.3
2	21	47.6	195.5
3	23	48.8	239.2
4	17	36.1	163
5	21	48.1	213

4. Supplementary References

1 Lin, S. et al. Covalent organic frameworks comprising cobalt porphyrins for catalytic CO2 reduction in water. *Science*. **349**, 1208-1213 (2015).

2 Zhang, Q. et al. Designing covalent organic frameworks with Co-O_4 atomic sites for efficient CO_2 photoreduction. *Nat. Commun.* **14**, 1147 (2023).

3 Ou, H. et al. Atomically dispersed Au-assisted C-C coupling on red phosphorus for CO_2 photoreduction to C_2H_6. *J. Am. Chem. Soc.* **144**, 22075-22082 (2022).

4 Huang, N. Y. et al. Electrostatic attraction-driven assembly of a metal–organic framework with a photosensitizer boosts photocatalytic CO_2 reduction to CO. *J. Am. Chem. Soc.* **143**, 17424-17430 (2021).

5 Wang, G. et al. Engineering a copper single-atom electron bridge to achieve efficient photocatalytic CO_2 conversion. *Angew. Chem. Int. Ed.* **135**, e202218460 (2023).

6 Xie, W.; Sun, W.; Chu, W.; Jiang, C.; Xue, Y. Investigation of the doped transition metal promotion effect on CO_2 chemisorption on Ni (111). *Appl. Surf. Sci.* **258**, 6239-6245 (2012).

7 Phung, Q. M.; Hagai, M.; Xiong, X. G.; Yanai, T. Polarization consistent basis sets using the projector augmented wave method: a renovation brought by PAW into Gaussian basis sets. *Phys. Chem. Chem. Phys.* **22**, 27037-27052 (2020).

8 Tao, J.; Zhang, Q.; Liu, T. Polaron formation and transport in Bi_2WO_6 studied by DFT+U and hybrid PBE0 functional approaches. *Phys. Chem. Chem. Phys.* **24**, 22918-22927 (2022).

9 Wang, G.; Chen, Z.; Wang, T.; Wang, D.; Mao, J. P and Cu dual sites on graphitic carbon nitride for photocatalytic CO_2 reduction to hydrocarbon fuels with high C_2H_6 evolution. *Angew. Chem. Int. Ed.* **61**, e202210789 (2022).

10 Xu, F.; Li, Z.; Zhu, R.; Chu, Y.; Pan, Z.; Xia, S.; Fu, J.; Xiao, Z.; Ji, X.; Liu, M.; Weng, B. Narrow band-gapped perovskite oxysulfide for CO_2 photoreduction towards ethane. *Appl. Catal. B Environ.* **316**, 121615 (2022).

11 Zhao, J. et al. Plasmonic control of solar-driven CO_2 conversion at the metal/ZnO interfaces. *Appl. Catal. B-Environ. 256*, 117823 (2019).

12 Lu, L. et al. Multifunctional Au/hydroxide interface toward enhanced C–C coupling for solar-driven CO_2 reduction into C_2H_6. *Inorg. Chem.* **62**, 2934-2941 (2023).

13 Yang, X.; Lan, X.; Zhang, Y.; Li, H.; Bai, G. Rational design of MoS_2@COF hybrid composites promoting C-C coupling for photocatalytic CO_2 reduction to ethane. *Appl. Catal. B-Environ.* **325**, 122393 (2023).

14 Xie, S.et al. Self-reconstruction of paddle-wheel copper-node to facilitate the photocatalytic CO_2 reduction to ethane. *Appl. Catal. B-Environ.* **310**, 121320 (2022).

15 Sorcar, S. et al. CO_2, water, and sunlight to hydrocarbon fuels: a sustained sunlight to fuel (Joule-to-Joule) photoconversion efficiency of 1%. *Energy Environ. Sci.* **12**, 2685-2696 (2019).

16 Wang, Y. et al. Synergy between plasmonic and sites on gold nanoparticle-modified bismuth-rich bismuth oxybromide nanotubes for the efficient photocatalytic C-C coupling synthesis of ethane. *J. Collid. Interf. Sci.* **616**, 649-658 (2022).

17 Fan, J. et al. Light-induced structural dynamic evolution of Pt single atoms for highly efficient Pphotocatalytic CO_2 reduction. *ACS Appl. Mater. Interfaces.* **14**, 26752-26765 (2022).

18 Fan, J. et al. Integrating Au@TiOx and Co sites in a tandem photocatalyst for efficient C-C coupling synthesis of ethane. *J. CO_2. Util.* **67**, 102333 (2023).

19 Ji, J. et al. Highly selective photocatalytic reduction of CO_2 to ethane over Au-O-Ce sites at micro-interface. *Appl. Catal. B-Environ. 321*, 122020 (2023).

20 Pan, W. G.; Li, C. F.; Zhang, Z. R.; Wu, T.; Guo, R. T. Efficient CO_2 reduction under visible light: Synergistic effects of Cu nanoparticles and Ni single atoms. *Appl. Catal. B-Environ.* **343**, 123492 (2024).

21 Xiong, W. et al. Highly stable lead-free perovskite $Cs_2AgBiBr_6$/UiO-66 Z-scheme heterostructures with enhanced photocatalytic activity for CO_2 photoreduction and organic dyes degradation. *Appl. Surf. Sci.* **644**, 158807 (2024).

22 Jia, J. et al. Nickel selenide/g-C_3N_4 heterojunction photocatalyst promotes C-C coupling for photocatalytic CO_2 reduction to ethane. *J. Colloid. Interf. Sci. 658*, 966-975 (2024).